

# The composition of the deep continental crust inferred from geochemical and geophysical data

Laura G. Sammon<sup>1</sup>, William F. McDonough<sup>1,2</sup>, Walter D. Mooney<sup>3</sup>

<sup>1</sup>Department of Geology, University of Maryland, College Park, MD 20742, USA

<sup>2</sup>Department of Earth Sciences and Research Center for Neutrino Science, Tohoku University, Sendai

980-8578, Japan

<sup>3</sup>Earthquake Science Center, United States Geological Survey, Menlo Park, CA 94025

## Key Points:

- We present a global model for the composition of the deep continental crust constrained by geochemical and geophysical data
- Crustal SiO<sub>2</sub> content decreases with increasing depth, and compositions correlate to relative depth rather than absolute depth
- Moho heat flux is predicted at  $18.8 \pm 8.8 \text{ mW/m}^2$  for stable continent regions

Author ORCID numbers are

Laura G. Sammon : 0000-0002-4538-0700

William F. McDonough : 0000-0001-9154-3673

Walter D. Mooney : 0000-0002-5310-3631

---

Corresponding author: Laura G. Sammon, lsammon@umd.edu

16      **Abstract**

17      Combining geochemical and seismological models constrains the composition of the middle  
 18      and lower continental crust better than either field can achieve alone. The inaccessible nature  
 19      of the deep crust (typically >15 km) forces reliance on analogue samples and modeling  
 20      results to interpret its bulk composition, evolution, and physical properties. A common  
 21      practice relates major oxide compositions of small- to medium-scale samples (e.g. medium  
 22      to high metamorphic grade terrains and xenoliths) to large scale measurements of seismic  
 23      velocities ( $V_p$ ,  $V_s$ ,  $V_p/V_s$ ) to determine the composition of the deep crust. We provide a  
 24      framework for building crustal models with multidisciplinary constraints on composition.  
 25      We present a global deep crustal model that documents compositional changes with depth  
 26      and accounts for uncertainties in Moho depth, temperature, and physical and chemical  
 27      properties. Our 3D deep crust global compositional model uses the USGS global seismic  
 28      database (Mooney, 2015) and a compilation of geochemical analyses on amphibolite and  
 29      granulite facies lithologies (Sammon & McDonough, 2021). We find a compositional gradient  
 30      from  $61.2 \pm 7.3$  to  $53.8 \pm 3.0$  wt.% SiO<sub>2</sub> from the middle to the base of the crust, with the  
 31      equivalent lithological gradient ranging from quartz monzonite to gabbronorite. In addition,  
 32      we calculate trace element abundances as a function of depth from their relationships to  
 33      major oxides. From here, other lithospheric properties, such as Moho heat flux, are derived  
 34      ( $18.8 \pm 8.8$  mW/m<sup>2</sup>). This study provides a global assessment of major element composition  
 35      in the deep continental crust.

36      **Plain Language Summary**

37      Using many different geophysical and geochemical techniques together helps us under-  
 38      stand the composition of the bottom two-thirds of the continental crust. We cannot sample  
 39      much of the continental crust directly because of how deep it is. Instead, we rely on rocks  
 40      that have been brought to the surface and measurements of the speed of seismic waves trav-  
 41      eling through the crust in order to determine what the deepest parts of the crust are made  
 42      of. Accounting for various factors, such as crust temperature and tectonic setting, allows us  
 43      to create a large-scale model for the composition of the deep crust.

44      **1 Introduction**

45      The deepest parts of Earth's crust are widely inaccessible to traditional geochemical  
 46      sampling and so their composition is poorly understood. Only in areas where eruptions have  
 47      brought xenoliths to the surface or where tectonic activity has exhumed medium and high  
 48      grade metamorphic terrains are we able to *partially* determine the composition of the deep  
 49      (middle and lower) continental crust. Even so, these *ex situ*, aged, weathered, and trans-

ported rocks may not adequately represent the overall, current composition of the deep crust. Such inaccessibility has challenged geochemists for decades, leading to competing models for continental crust and bulk silicate Earth (BSE) compositions, formation, and evolution. Dissonance in the geochemical community stems from known and unknown unknowns; that is, we are mostly certain of the uncertainties in our geochemical and petrological measurements, but we are uncertain if our samples are truly representative of large swathes of the deep crust or if they are merely point samples. Xenoliths and terrains are the sum of the processes that form them, which may cause them to differ from what is presently 15–45 km and deeper. The deep crust is an enigma, and compositions of xenoliths and high grade metamorphic terrains provide only an incomplete cipher.

Seismological techniques, however, provide another piece of the cipher by directly measuring the physical state of large sections of the deep crust. Physical properties (e.g. density, Poisson's ratio,  $V_p$ , and  $V_s$ ) determined from these *in situ* geophysical experiments can be compared to laboratory experiments on rocks of known compositions, particularly medium to high grade metamorphic lithologies (amphibolite and granulite facies lithologies) to place constraints on estimates of deep crustal composition. Integrating geochemical and geophysical observations, related to each other by empirically (laboratory) derived thermodynamic properties, provides a reinforced, clearer, consistent picture of middle and lower crustal composition.

This study uses geophysical and geochemical datasets to build a global compositional model of the lower two-thirds of the continental crust. We generate a composition versus depth model for the middle and lower continental crust by applying thermodynamic modeling software to medium and high grade lithologies. We then compare the thermodynamically-generated seismic velocities to velocities obtained from seismological measurements to produce a jointly constrained geochemical-seismological compositional model.

## 2 Methods

Our model calculations are split into two main parts: 1) assembling data and performing thermodynamic calculations, and 2) adjusting model parameters to generate deep crustal compositional models with uncertainties. These calculations require seismic velocity depth profiles, Moho depths, and crustal temperature gradients for the areas of interest. Using the thermodynamic modeling software *Perple\_X*, we calculate the probability that different deep crustal compositions could produce the observed seismic signal. These calculations are conducted using our modeling software, *CrustMaker*, which is provided as an electronic supplement. The calculation adopts a subdivision of the global continental crust into 13 tectonic regimes (Figures 1 and 2) to speed calculations and extrapolate results to areas with

lower data coverage. The resolution of this global model is set to  $1^{\circ}$ latitude x  $1^{\circ}$ longitude x 3 km depth as a default, but can be changed in the model to suit user needs. We chose this default resolution for our global model based on the resolution of our crustal categories (each  $1^{\circ} \times 1^{\circ}$  of crust was assigned a tectonic regime based on models such as CRUST1.0, Litho1.0, and modifications discussed further in Section 2.1), and the resolution of our crustal thickness and temperature data, the ramifications of which are discussed further in the Results section. For considering higher resolution, regional scale data, the same methods can be used. Instead of simplifying the crust into tectonic regimes, calculations are run for individual seismic velocity profiles, so that if there are, for example, 34 seismic velocity profiles as inputs, there will be 34 locations for which compositional profiles are generated.

We calculated the overlapping probability between measured seismic velocities and the Perple\_X-derived velocities for amphibolites and granulites equilibrated at middle and lower crustal pressures and temperatures (assuming an average crustal density of  $2900 \pm 200$  kg/m<sup>3</sup> (Wipperfurth et al. (2020), c.f. Christensen and Mooney (1995)). Integrating the area under both curves, the area shown as magenta in Figure 3, for a sample of composition  $X$  yields the total probability of sample  $X$  producing the observed seismic signal. Repeating this technique for a multitude of sample compositions at various depths and temperatures yields a final Monte Carlo model for deep crustal composition. Probability distributions are generated for Vp, Vs, and Vp/Vs and then multiplied together to constrain further the final probability.

## 2.1 Model Inputs

A global model of Vp, Vs, and Vp/Vs was generated from a compilation of over 8700 (Vp) and 1000 (Vs) 1-D seismic velocity profiles obtained from the Global Seismic Catalog (GSC) database (Mooney, 2015). Both controlled and passive source seismic velocity profiles were included to increase data coverage. We included only profiles with both Vp and Vs data that had been sampled at a minimum of 5 depth intervals within the crust. Figure 2 shows our tectonic regimes and the location of each seismic velocity profile used. We used global Moho depths from Litho1.0, except on the continental margins, where we reference Szwilus et al. (2019) Moho values. In comparison to Litho1.0, Szwilus et al. (2019) incorporated a larger dataset on the continental margins ( $\sim 1600$  profiles) and did not average depths across the continent-ocean transition. Global Moho temperatures were generated from the TC15 global temperature model of Artemieva (2006). We assumed a linear temperature gradient within the continental crust, though we address the contributions from crustal heat production in a later section of this paper.

The foundation of the tectonic regimes chosen for this global model are the classifications of crust provided by the Crust family of models (Mooney et al., 1998). To further identify tectonic provinces and group together geophysically similar crust, we incorporated crustal thickness, seismic velocity ( $V_p$ ,  $V_s$ ), gravity anomaly, sediment thickness, crust elevation, and surface heat flux observations in a tSNE test (t-distributed stochastic neighbor embedding, perplexity of 50). Results generally favored grouping the continental crust into 8 - 12 regimes, mostly matching the designations already given in Crust1.0. We augmented these regimes with additional groupings, such as “Thinner Himalyan” crust, when it became clear that the seismic velocity structure of the perimeter of the Himalayas differed from the thickest Himalaya, the Tethyan region, and paleo-orogenies. Areas with sparse seismic coverage such as central South America, northern Africa, rely heavily on extrapolation of measurements from similar tectonic regimes. Average  $V_p$  and  $V_s$  profiles for most tectonic regimes were created from a distribution of tens to hundreds of individual measurements (Table 1). A notable exception is the “Continental Margins” regime, which was represented by an astounding  $> 1,600$  profiles. Highly localized regimes, such as Andean or Himalayan crust, tended to have  $< 100$  profiles due to the uniqueness of their crustal profiles.

Figure 1 and Table 1 show the proportion of different crustal regimes by surface area coverage. These tectonic provinces consider only crust exposed at the surface, so that regimes such as “Platform” have underlying crystalline crust that may be Proterozoic or Archean in age. The Proterozoic crust covers the largest fraction (32%) of the continental crust, followed by continental margins (16%).

A compilation of amphibolite and granulite facies major and trace element abundances (Sammon & McDonough, 2021) serves as our geochemical constraint on the deep (middle and lower) continental crust. We modeled amphibolite facies lithologies for the middle third of the crust and granulite facies lithologies for the bottom third, in agreement with the depth assignment of Rudnick and Gao (2014). We cannot confidently determine which portions of the deep crust are more appropriately represented by amphibolite versus granulite facies data with our current model. In theory, one metamorphic grade would have greater overall overlap with the seismic velocity profile(s), thus determining which is the more accurate rock type to use. In practice, however, amphibolite and granulite facies lithologies of the same  $\text{SiO}_2$  abundance tend to have similar seismic velocities (see Section 3.1). As such, we have assumed that the metamorphic grade switches from amphibolite to granulite at  $2/3$  the crustal depth. Future studies should investigate using anisotropy in the deep crust to further establish lithology. Though trace elements do not participate in thermodynamic calculations, we were able to estimate trace element abundances based on a joint probability analysis with the mineral-forming major oxides. Samples were placed into bins based on

155 the abundance of the oxide and trace element of interest (e.g. SiO<sub>2</sub> and U). Bin width was  
 156 selected using Sturges rule ( $N_{bins} = \log_2(N) + 1$ ). For each major oxide composition bin,  
 157 there was then a correlated trace element abundance distribution.

## 158 2.2 Model Uncertainties

159 Errors in the seismic and geochemical inputs will skew results. It is imperative to un-  
 160 derstand the uncertainties in the input datasets if we want a clean picture of the uncertainty  
 161 of our crustal composition models.

162 The program also will not assess the model error stemming from foundational assump-  
 163 tions about what types of lithologies should be used as geochemical inputs and the tectonic  
 164 regimes assigned to global crust. These two assumptions are expected to control the sys-  
 165 tematic error of the model, which is why we made the program flexible and modular. Our  
 166 approach facilitates testing different fundamental crustal models and highlights the pro-  
 167 jected differences in crust composition.

168 The primary sources of model error stem from uncertainty in the crustal temperature  
 169 gradient and Moho depth. Again, these are parameters that can be set by the user. For  
 170 our preferred model, the uncertainty on Moho depth is on the order of 10% or less in most  
 171 areas of the global model. The temperature uncertainty is much greater. Global Moho  
 172 temperatures are taken from Artemieva (2006), which reports no uncertainties. Therefore,  
 173 uncertainty is taken as the standard deviation of all temperatures found within a given  
 174 crustal regime (regimes discussed below), and the model runs a number of Monte Carlo  
 175 iterations to produce a distribution of Moho depths and temperatures. Future results could  
 176 be improved with Moho temperature models that quantify uncertainty more directly.

177 We have also attempted to mitigate the bias introduced by the oversampling of particu-  
 178 lar geochemical compositions. An oversampled composition, such as 100 input compositions  
 179 with nearly identical major oxide content artificially inflates the probability of that compo-  
 180 sition in our final combined model. However, we do consider the reporting of compositions  
 181 to be at least somewhat reflective of the proportion of rock types present in the deep crust,  
 182 i.e. if the distribution of reported compositions is bimodal, the rocks in the deep crust are  
 183 likely bimodal in composition. Therefore, we only considered a sample redundant if its oxide  
 184 content differed from another's by < 3 wt.% (9 major oxides, using the distance between  
 185 vectors formula  $d = \sqrt{x_1^2 + x_2^2 + \dots + x_n^2}$ , where  $x_n$  is the difference in wt.% of an oxide  
 186 between two samples), and its Perple\_X generated values for Vp, Vs, and Vp/Vs were within  
 187 uncertainty of each other.

188        The internal error contributed by calculational uncertainty is minimal. The overlap  
 189        between of seismic velocity measurements and Perple\_X-derived seismic velocities is calcu-  
 190        lated via trapezoidal numerical integration at intervals determined by the uncertainty in  
 191        the seismological data. When the interval is too large to use for the integration, the pro-  
 192        gram reduces the interval by half. The precision errors of Perple\_X are generally negligible  
 193        compared to the uncertainty on our other inputs (Connolly, 2005).

### 194        2.3 Quality, Expense, and Time: Global vs. Local Models

195        In numerical modeling, there is often a tradeoff between computation time and model  
 196        resolution. For a global perspective of the continental crust, breadth and total model cov-  
 197        erage may be more valuable than high data resolution, especially if results can be averaged  
 198        over large areas. This large-scale, globe-encompassing model, however, comes with the  
 199        choice of either short computation time and low resolution or longer computation time and  
 200        higher resolution. Alternatively, those interested in a more in-depth analysis of a localized  
 201        region may be able to accommodate higher resolution models. We suggest considering the  
 202        following when determining whether to use a global or local scale model: data resolution  
 203        (especially in seismic velocity profiles), data coverage, and model application. Those with  
 204        data resolution on the scale of  $> 0.5^\circ \times 0.5^\circ$  should consider using the global version of the  
 205        script. Those with higher resolution, such as that provided by the Earthscope USArray, the  
 206        AUSArray, or the J-ARRAY, should use the regional scale model. For the remainder of this  
 207        study, we will analyze global model results. Sammon et al. (2020) presents an example of a  
 208        local-scale composition analysis using a nascent version of this method.

## 209        3 Results

### 210        3.1 Empirical Composition-Velocity Trends

211        Seismic velocities correlate with  $\text{SiO}_2$  content because of the high abundance of  $\text{SiO}_2$   
 212        in granulite and amphibolite facies lithologies compared to all other oxides. Perple\_X-  
 213        calculated  $V_p$  and  $V_s$  values at given pressure-temperature conditions show a quadratic  
 214        relationship between  $\text{SiO}_2$  and velocity (Figures 4 and 5). The coefficients of the quadratic  
 215        are determined for a given pressure and temperature, and are ultimately correlated to the  
 216        empirical mineral physics datasets used in the Perple\_X Gibbs free energy minimization.  
 217        Amphibolite and granulite facies lithologies span similar  $V_p$  and  $V_s$  values, though the  
 218        shapes of their distributions are marginally different. This is because their mineralogies are  
 219        similar, both being dominated by plagioclase, garnet, and pyroxene, all of which have  $V_p$  of  
 220         $\sim 7$  km/s and  $V_s$  of  $\sim 3.6$  km/s. Despite considerable scatter in the  $V_s$  data, when paired  
 221        with  $V_p$ , a clear trend emerges: increasing  $\text{SiO}_2$  leads to decreasing velocities.

222 Higher Vp's correlate to lower silica content (Figures 6A and B). Higher Vp/Vs ratios  
 223 also have decreased silica content, though for a given SiO<sub>2</sub> percentage, there is roughly a 10%  
 224 spread in Vp/Vs. A slight curve in the amphibolite facies data becomes more pronounced  
 225 in the granulites, developing an arcuate shape in the Vp/Vs vs. Vp plot. The same trends  
 226 appear when analyzing Vp/Vs vs. Vs (Figures 6C and D), though the data is more acutely  
 227 curved. For both amphibolite and granulite lithologies, increasing Vs can lead to either  
 228 an increase or a decrease in Vp/Vs ratio. The maximum Vp/Vs for amphibolite facies  
 229 lithologies at typical middle crustal P-T conditions, is expected at a Vs of about 3.5-3.8  
 230 km/s, a Vp of 6.5-7 km/s, and SiO<sub>2</sub> of 55 wt.%. For granulite, this maximum is expected  
 231 at compositions closer to 60-63 wt.% SiO<sub>2</sub>. Interestingly, the maximum Vp/Vs in granulite  
 232 lithologies corresponds to the lowest Vs rather than the highest Vp, suggesting that Vs  
 233 variations exert a stronger control on Vp/Vs ratios than does Vp.

### 234 3.2 Deep Crustal Density

235 We calculated deep crustal density by tracing the Vp and Vs values from Perple\_X that  
 236 overlapped with our seismological database back to their input samples. Then, instead of  
 237 reporting the composition, we report the Perple\_X-derived density of those input samples.  
 238 We found that, similar to composition, deep crustal densities among the different tectonic  
 239 provinces correlated much more closely when normalized to crustal thickness (Figure 7). The  
 240 density uncertainty for each regime was 3%, a number that reflects the velocity uncertainties  
 241 of our seismic velocity profiles. Deep crustal density ranges from 2700-2780 kg/m<sup>3</sup> at 13 km  
 242 depth to 3290-3340 kg/m<sup>3</sup> at the Moho.

243 We note that, in order to calculate deep crustal pressure, and thus mineralogy and  
 244 composition, we *already assumed* a bulk crustal density of 2900 kg/m<sup>3</sup>. This initial assumption,  
 245 though, does not greatly affect our composition results because there is, at most, a  
 246 calculated pressure difference of <15% caused by using the 2900 kg/m<sup>3</sup> a-priori density vs.  
 247 our model-generated density. This <15% pressure difference does not greatly change the  
 248 stable mineral assemblages or velocities calculated by Perple\_X for the deep crust.

### 249 3.3 Composition

250 Our main analysis focuses on SiO<sub>2</sub> abundance and its uncertainties because of its strong  
 251 correlation to seismic velocities. The SiO<sub>2</sub> content at typical middle and lower crust depth  
 252 intervals (Figure 8) is given in Table 2. All 9 major oxide inputs (SiO<sub>2</sub>, TiO<sub>2</sub>, Al<sub>2</sub>O<sub>3</sub>, CaO,  
 253 MgO, FeO<sub>T</sub>, MnO, K<sub>2</sub>O, Na<sub>2</sub>O) can be found in Table 3 and corresponding maps in Sup-  
 254 plement Section 3. We use the notation “M<sub>x</sub>”, where x is the percent distance to the Moho  
 255 (M) from the surface, to indicate depth on our figures so that tectonic regimes with varying

256 crustal thicknesses are comparable. The deep crust starts at an intermediate composition,  
257 globally ranging from 58 - 68 wt.% SiO<sub>2</sub>, and the bulk deep crust gradually transitions to  
258 50-55 wt.% SiO<sub>2</sub> as it approaches the Moho (Figure 9). Global scale SiO<sub>2</sub> composition of  
259 the continental crust mostly decreases (or remains steadily mafic) with increasing depth for  
260 all tectonic regimes (Figure 10). Uncertainty in global SiO<sub>2</sub> also decreases with increasing  
261 depth due to fewer samples fitting the seismic signal in most cases. In the Andean and Hi-  
262 malayan tectonic regimes, however, the uncertainty tends to be larger than in other regions  
263 because of both the variation in geochemical data fitting the seismic signal and the rela-  
264 tive sparsity of seismological profiles that sample the deepest parts of these thick tectonic  
265 regimes.

266 CaO content of the deep crust is also of interest due to its absolute abundance and  
267 significance as a contributor to sedimentary deposits, though only siliciclastic rocks and not  
268 carbonates were considered viable deep crust components (Wilkinson et al., 2009; Hartmann  
269 et al., 2012). In our model, Ca is mostly contained in plagioclases, pyroxenes, and garnets.  
270 CaO abundance tends to increase with depth because of the increasingly mafic nature of the  
271 deep crust, and therefore regions of low SiO<sub>2</sub> correlate with regions of high CaO. Globally,  
272 the median CaO at crustal depths of M<sub>85</sub> is 9.1 ± 3.1 wt.% (Figure 11).

273 We can also derive the global distribution of a trace element if that trace element has  
274 a quantifiable relationship to one of the thermodynamic components (major oxides) used  
275 in our model. We used a geochemical database of samples with both major and trace  
276 element concentrations (Sammon & McDonough, 2021) to generate trace element maps as  
277 a function of major oxide abundance. We used a bivariate probability analysis to generate  
278 trace element distributions from a major oxide abundance, such as SiO<sub>2</sub>, at a specific depth  
279 or location. Although we suggest using regional analyses for high resolution interpretations  
280 of trace element abundance, we present here global predictions and uncertainties for Sr  
281 (Figure 12) and U (Figure 13) content based on their relationships with CaO and SiO<sub>2</sub>,  
282 respectively, as examples. Global average Sr increases with increasing CaO until plagioclase  
283 is no longer the dominant Ca-bearing mineral. Uncertainties on global U concentration span  
284 an order of magnitude because the abundance of U in a given metamorphic sample ranges  
285 from a few hundreds of ppb to a few ppm. U and SiO<sub>2</sub> abundances, however, are positively  
286 correlated, with median U increasing as median SiO<sub>2</sub> increases.

287 **4 Discussion**288 **4.1 SiO<sub>2</sub> and Overall Deep Crustal Composition**

289 Figure 10 shows steady or decreasing SiO<sub>2</sub> with increasing depth. Figure 8 also makes  
 290 it apparent, though, that the absolute SiO<sub>2</sub> at a given depth is not equal across different  
 291 crustal types. For example, “Extended” crust appears mafic at 30 km depth while the  
 292 “Thick Himalayan” crust is felsic at that depth, and “Proterozoic” crust falls in between  
 293 (Figure 8). However, a more laterally consistent trend appears when comparing percent of  
 294 the crustal column traversed rather than absolute depth (Figure 8). Most regions show a  
 295 5-10 wt.% decrease in median SiO<sub>2</sub> through the deep crust regardless of crustal thickness,  
 296 so that SiO<sub>2</sub> decreases much faster in areas of thin crust than in areas of thick crust. We  
 297 predict the global median SiO<sub>2</sub> at 50% above the Moho (or, alternatively, 50% crustal  
 298 column thickness) to be  $61.2 \pm 7.3$  wt.% SiO<sub>2</sub> with CIPW normative mineralogy of <10  
 299 wt.% alkali feldspar <15 wt.% quartz. The middle continental crust is therefore expected  
 300 to resemble a quartz monzonite; the lower crust, with  $53.8 \pm 3.0$  wt.% SiO<sub>2</sub> and  $9.1 \pm 3.1$   
 301 wt.% CaO, is expected to transition to a gabbro-norite.

302 Density sorting provides a simple mechanism for producing the compositional structure  
 303 of the continental crust. The process of crustal genesis leaves mafic, restitic material at the  
 304 base of the crust regardless of crustal thickness except in the few cases discussed in the  
 305 next paragraph. More buoyant, felsic material ascends to the top of the crust, producing a  
 306 gradient of SiO<sub>2</sub> that scales with crustal thickness. Without density sorting, the deep crust  
 307 could be more mafic because it is simply closer to the mantle and therefore has a greater  
 308 number of mafic intrusions. Our results do not indicate any need for sharp compositional  
 309 boundaries in the deep crust. The  $M_X\%$  notation reinforces the importance of scaled, relative  
 310 depth in the crust rather than absolute depth for making compositional comparisons.

311 Two regions that appear conspicuously more felsic than the global deep crustal median  
 312 are the Andes and the Thin Himalayan crust (Figure 10). A low temperature gradient could  
 313 once again be the cause of this compositional difference, but we also must consider two  
 314 other possibilities, particularly around the northern and northeastern Tibetan Plateau and  
 315 Himalayan ramp. The first is that thick, convergent margins, especially in the Himalayas,  
 316 might have layers of upper crustal material thrust deeper within the crust. In contrast,  
 317 underthrust upper crustal material is less likely to appear in the Andes, which is a continent-  
 318 ocean subduction zone. Alternatively, pockets of melt and partially melted material in the  
 319 Andean middle and lower crust could reduce the shear wave velocity (Nelson et al., 1996;  
 320 Regis et al., 2016; Searle et al., 2009; Caldwell et al., 2009; Schmitz et al., 1997; Schilling &

321 Partzsch, 2001). Because our current model does not factor in melt, slower Vs speeds would  
322 be attributed to a more felsic composition.

323 Other anomalous regions in Figure 8, particularly the continental margins of Antarctica,  
324 the East African rift zone, and the Sea of Japan, are likely caused by inaccurate temperature  
325 and Moho inputs. The East African Rift could appear felsic because the model’s temperature  
326 gradient for that actively rifting region is too low; a cooler felsic composition can produce  
327 the same velocities as a warmer mafic composition. On the other hand, the highly localized,  
328 extremely felsic borders around Antarctica and between Japan and China likely indicate  
329 a misclassification of crust type and/or Moho depth. Thinner, oceanic crust has been  
330 documented in both regions (Hirata et al., 1992; Cho et al., 2004; Gohl, 2008; McCarthy et  
331 al., 2020). Better Moho and temperature resolution of the ocean-continent transition should  
332 increase the accuracy of compositional models in these regions.

333 Mafic granulite lithologies reach gravitational instability in the lower 10-20% of the  
334 average crustal column (Jagoutz et al., 2011), surpassing the upper mantle’s density of  
335 3300 kg/m<sup>3</sup>. Therefore, according to Figure 7, most of the granulite facies lower crust  
336 for continental margins, Andean crust, Tethyan crust, and Phanerozoic crust should be  
337 gravitationally unstable. On the other hand, most other tectonic regimes would just reach  
338 mantle-like densities around the Moho depths. Thinner Himalayan type crust has a middle  
339 crustal density ~9% lower than other regimes, correlating with negative seismic velocity  
340 anomalies. Arcs have the next lowest densities on average, suggesting that the denser lower  
341 crustal crust beneath some arcs has already founded (Jagoutz et al., 2011). The accreted  
342 arc of the “Andean” type crust in particular (pink triangles in Figure 7B) displays a stark  
343 decrease in density that has been associated with delamination of the lowermost crust (Kay  
344 & Kay, 1993; Ducea, 2011; Gao et al., 2021).

345 Forming continental crust via island arc processes, however, would then require the  
346 deep crust to become denser over time, since most of our crust regimes have lower crust  
347 calculated as denser than arcs. This can be achieved by cooling the crust, thickening it  
348 further, intra-crustal differentiation, or by mafic igneous injections into the lower crust. If  
349 our Moho temperature model is too hot, though, it will require denser, more mafic lower crust  
350 to explain the Vp and Vs values. As such, we note that the compositions discussed in the  
351 next section are intrinsically tied to Moho temperature, and may be skewed towards mafic  
352 granulites. Reducing the assumed crustal Moho temperatures would bring the estimated  
353 average crustal density closer to arc crust density.

354 There is a tradeoff between temperature and composition. Vp and Vs both carry a  
355 temperature dependence through their bulk and shear moduli, so accurate temperature

estimates are imperative for modeling the crust; decreased seismic velocities can be the result of either higher temperature or greater SiO<sub>2</sub> content. The results presented here uses a linear temperature gradient through the crust from the TC15 global temperature model (Artemieva, 2006).

Table 4 reports one composition for the middle and one for the lower continental crust, a practice that is required to make meaningful comparisons to previous crustal models. While we recognize the assumption of a three-layer crust as an oversimplification of the diversity of crustal compositions, it is useful for some calculations to have average composition numbers for the crust; for instance, mantle tomography studies which require crustal correction, crustal corrections for geoneutrino studies; models of Earth's thermal history; and planetary scale compositional model for comparison with other rocky bodies. Compositional models in Table 4 have been normalized to 100 wt.%. Our middle crustal composition falls between two possible compositions given by Hacker et al. (2015): the fastest Vp endmember composition for the middle crust (62.7 wt.% SiO<sub>2</sub>), and the middle crustal composition expected when the crust takes on a two compositional layer (upper and lower) structure, instead of three, (57.3 wt.% SiO<sub>2</sub>). These SiO<sub>2</sub> estimates overlap with the 62 wt.% SiO<sub>2</sub> reported by Christensen and Mooney (1995) and fall on the mafic side of the uncertainty of the 63.5 wt.% SiO<sub>2</sub> middle crust reported by Rudnick and Nyblade (1999). Similar trends persist throughout the other major oxides. Our proposed lower crust composition is in close agreement with the lower crust of Rudnick and Gao (2014) and other mafic estimates (e.g. Hacker et al. (2015)'s fast Vp lower crust; Jagoutz and Schmidt (2012)). Models which predict a more intermediate-felsic lower crust, such as the North China craton lower crustal model of Liu et al. (2001) or the higher SiO<sub>2</sub>, lower Vp options listed by Hacker et al. (2015), are not consistent with our global average, though isolated regions of more felsic lower crust may exist.

## 4.2 CaO and Sr

Bulk CaO concentration increases with depth (Figure 11) but as a component of mafic, siliciclastic rocks, not carbonate. This is due in part to our imposed amphibolite/granulite grade lithology restrictions on possible deep crust composition, but is reinforced by high density and Vp values observed in the deep crust. Carbonates, with deep crustal densities of approximately 2750 kg/m<sup>3</sup> and Vp's of 6.6 - 6.8 km/s (Christensen & Mooney, 1995), cannot substantially contribute to the deep crust. There are also few carbonate-dominated granulite facies xenoliths and terrains compared to the number of silicate granulites. A comparison of Figures 8B and 11 shows good correlation globally between regions of high SiO<sub>2</sub> and low CaO. Uncertainties in CaO track the same trends as SiO<sub>2</sub> as well, though the

391 relative % uncertainty is roughly 10% higher on CaO than on SiO<sub>2</sub> because CaO does not  
 392 follow velocity trends as cleanly as SiO<sub>2</sub>.

393 CaO content does, however, predictably track with Sr concentration (Figures 11 and  
 394 12). Sr abundances cannot be directly derived from velocity calculations, but it can be  
 395 predicted from its geochemical relationship with CaO. Patterns emerge when comparing the  
 396 global distribution of Sr and CaO from two distinct sources: equilibrium mineralogy and  
 397 data binning. First, Sr abundance increases for CaO contents between 2-6 wt.%, reaching  
 398 a maximum at about 500 ppm Sr. However, Sr gradually decreases to 350 ppm as CaO  
 399 increases to >6 wt.%. This shift in Sr abundance corresponds with the transition from  
 400 plagioclase as the only Ca-bearing mineral phase to the addition of garnet and clinopyroxene  
 401 as stable Ca-bearing phases.

402 Second, we see sharp jumps in Sr abundance in neighboring tectonic regions as a con-  
 403 sequence of our data binning (Figure 12). The uncertainty on CaO content dictates that  
 404 the compositional bin-widths are as wide as 2-3 wt.% for a total of six bins. Each bin has  
 405 a central Sr value and distribution, leading to six possible median Sr abundances. The  
 406 uncertainties on Sr are a combination of the systematic uncertainty (which CaO bin) and  
 407 the statistical uncertainty (Sr variation within each bin) associated with each latitude by  
 408 longitude voxel.

#### 409 4.3 Heat Production and Moho Heat Flux

410 Low heat production is predicted for the bulk deep crust ( $\sim 0.15$  nW/kg or  $\sim 0.43$   
 411  $\mu\text{W}/\text{m}^3$ , assuming  $2900 \text{ kg/m}^3$ ) (Fountain et al., 1987; Kukkonen et al., 1997; Jaupart et  
 412 al., 2016). Areas with high predicted SiO<sub>2</sub>, such as the Andes and continental margins,  
 413 have estimated U content up to 4x higher than the global M<sub>85%</sub> median (U = 0.173 ppm)  
 414 because of the correlation between high SiO<sub>2</sub> samples and high U. Uncertainties on the  
 415 global scale remain substantial and range by an order of magnitude. For this reason we  
 416 recommend using regional heat producing element (HPE) data for understanding smaller  
 417 scale variations and reserve this study's results for continent- or global-scale models. Using  
 418 the methods discussed in the previous sections, we derived U abundance from SiO<sub>2</sub>, and  
 419 assume Th/U<sub>mass</sub> of  $3.77 \pm 0.1$  (Wipperfurth et al., 2018; Sammon & McDonough, 2021)  
 420 at M<sub>85%</sub> depth. Combining U and Th with K<sub>2</sub>O abundance, we calculated an expected  
 421 M<sub>85%</sub> heat production of 0.056 nW/kg ( $0.19 \mu\text{W}/\text{m}^3$ , assuming  $2900 \text{ kg/m}^3$ ). Figure 14  
 422 shows global heat production values, which are consistent with Huang et al. (2013); Rudnick  
 423 and Gao (2014). Our model is also consistent with local studies based on HPE analyses  
 424 of deep crustal xenoliths, such as Gruber et al. (2021); Pinet and Jaupart (1987); Ashwal  
 425 et al. (1987). The uncertainties on this global model are dominated by uncertainties on

426 U abundances. Even so, our *uncertainty on the median or central value* of HPEs or heat  
 427 production is well constrained at  $\pm 0.1\%$ . While possible heat production values span an  
 428 order of magnitude, the median/average heat production value is better constrained.

429 Given density, composition, surface heat flux (Lucaleau, 2019; Shen et al., 2020) pa-  
 430 rameters (Table 5), and an average thermal conductivity for crustal rocks (i.e., 2.65 W/m/K;  
 431 Miao et al., 2014), we can generate a model prediction for the global Moho heat flux:

$$Q_M = Q_0 - (H_{crustal} * z_{crustal})$$

432 where  $Q_0$  is surface heat flux ( $\text{W}/\text{m}^2$ ),  $H_{crustal}$  is crustal heat production ( $\text{W}/\text{m}^3$ ),  $z_{crustal}$   
 433 is the crustal thickness (m), and  $Q_M$  is Moho heat flux ( $\text{W}/\text{m}^2$ ), with only vertical variations  
 434 in heat flux being considered. Figure 15 shows the expected Moho heat flux based on our  
 435 deep crustal model and a Gaschnig et al. (2016) model for the upper crust composition.

436 The median global continental Moho heat flux, shown in Figure 15, is  $24.8 \pm 11.9$   
 437  $\text{mW}/\text{m}^3$ . However, if we consider only tectonically stable regions, the median Moho heat flux  
 438 is  $18.8 \pm 8.8 \text{ mW}/\text{m}^3$ , though, both values overlap with stable continent estimates (Jaupart  
 439 et al., 2007). The Moho heat flux calculations depends substantially on the assumed HPE  
 440 abundance model for the upper crust, as it contributes  $\sim 60\%$  of the total crustal heat  
 441 production in most regions. The middle crust, while not as HPE enriched as the upper  
 442 crust, still produces about 30% of crustal heat production. The mafic lower crust produces  
 443  $< 10\%$ . Pairing an upper crustal composition of Gaschnig et al. (2016) with our deep crustal  
 444 composition yields a reasonable Moho heat flux for tectonically stable regions and agrees  
 445 with the prediction by Jaupart et al. (2007), but marginally so for models having on average  
 446 a slow  $V_p$  crust structure (Hacker et al., 2015). Using these upper crustal U and Th  
 447 abundances in low heat flux areas, though, particularly cratonic regions, results in roughly  
 448 6% (by area) of the continents having a negative heat flux across the Moho (an unreasonable  
 449 condition) – or more likely, other factors, such as heat dissipation through fluid circulation  
 450 in the near surface, are needed to explain these low surface heat flux regions (e.g., 20-40  
 451  $\text{mW}/\text{m}^2$ ). Alternatively, the assumed upper crustal heat production values may need to  
 452 be lowered, however, before making such adjustments further research is required. Most of  
 453 these low heat flux areas coincide with stable cratonic lithosphere, where low heat flux and  
 454 heat production is not a new observation (e.g., Nyblade and Pollack (1993); Kukkonen et  
 455 al. (1997); Jaupart et al. (2007); Cammarano and Guerri (2017)). Various studies estimate  
 456 cratonic crustal heat production to be between  $0.6$  and  $1 \mu\text{W}/\text{m}^3$  (Gruber et al., 2021;  
 457 Jaupart et al., 2016; Phaneuf & Mareschal, 2014; Mareschal & Jaupart, 2013; Jaupart et  
 458 al., 2014), so we approximate upper crustal heat production as  $0.8 \mu\text{W}/\text{m}^3$ , which is the

459 maximum permissible heat production value found by Rudnick and Nyblade (1999) for the  
 460 Kalahari craton and the maximum average crustal heat production expected for crust  $\geq 2$   
 461 Ga (Jaupart et al., 2016).

## 462 5 Conclusions

463 We have constructed a global model for the deep continental crust composition by syn-  
 464thesizing seismic, temperature, heat flux, and geochemical data. We predict deep crustal  
 465 compositions on the global scale using major and trace element compositions from amphi-  
 466 bolite and granulite facies lithologies, and seismic velocity profiles. Our proposed global  
 467 compositional model uses a USGS database of crustal seismic studies, published composi-  
 468 tions for thousands of medium and high grade metamorphic rocks, and constraints on Moho  
 469 depth (Pasyanos et al., 2014; Szwilus et al., 2019), crust temperature (Artemieva, 2006),  
 470 and surface heat flux (Lucazeau, 2019; Shen et al., 2020).

471 V<sub>p</sub>, V<sub>s</sub>, and V<sub>p</sub>/V<sub>s</sub> correlate well with bulk rock SiO<sub>2</sub> content because of its high  
 472 abundance in rocks, and SiO<sub>2</sub> can be used as a predictor of velocity if temperature can  
 473 be estimated accurately. Globally, SiO<sub>2</sub> concentration tends to decrease with increasing  
 474 depth, leading to a predominantly mafic and intermediate-mafic base of the crust. The  
 475 decreased density and less mafic nature of the lower crust in younger and tectonically active  
 476 crust, such as arcs and active mountain ranges, suggests that they are hotter than our  
 477 temperature model predicts, that they have undergone lower crustal delamination, or both.  
 478 Global median SiO<sub>2</sub> content for the middle and lower crust are  $61.2 \pm 7.31$  and  $50.1 \pm 3.48$   
 479 wt.%, respectively, though steady composition and velocity gradients in the deep crust urge  
 480 us to embrace a less distinctly layered view of the crust. This mid-to-deep crustal gradient  
 481 in wt.% SiO<sub>2</sub> is the equivalent of a lithological gradient ranging from quartz monzonite to  
 482 gabbro-norite. We predict the abundances of multiple thermodynamic oxides, many of which  
 483 are correlated to trace element abundances. This correlation allows us to derive expected  
 484 heat production in the deep crust. We therefore also predict a Moho heat flux of  $18.8 \pm 8.8$   
 485 mW/m<sup>2</sup> for tectonically stable regions.

## 486 6 Author Contributions

487 LGS, WFM and WDM contributed to the conceptualization and methodological devel-  
 488 opment of this project. LGS did software development, modeling, visualization, and writing.  
 489 WFM and WDM contributed input and discussion throughout, as well as with the revising  
 490 and editing. WDM contributed the compilation of seismic surveys used to build this model.  
 491 All authors have read and approved this manuscript.

492 **Acknowledgments**

493 We gratefully acknowledge the support by NSF grants EAR1650365 and 2050374 to WFM  
494 and support from the United States Geological Survey Earthquake Hazards Program to  
495 WDM. We also thank Wolfgang Szwilus for his insights on heat flow modeling. Data and  
496 modeling software can be found at <https://doi.org/10.5281/zenodo.5087347>.

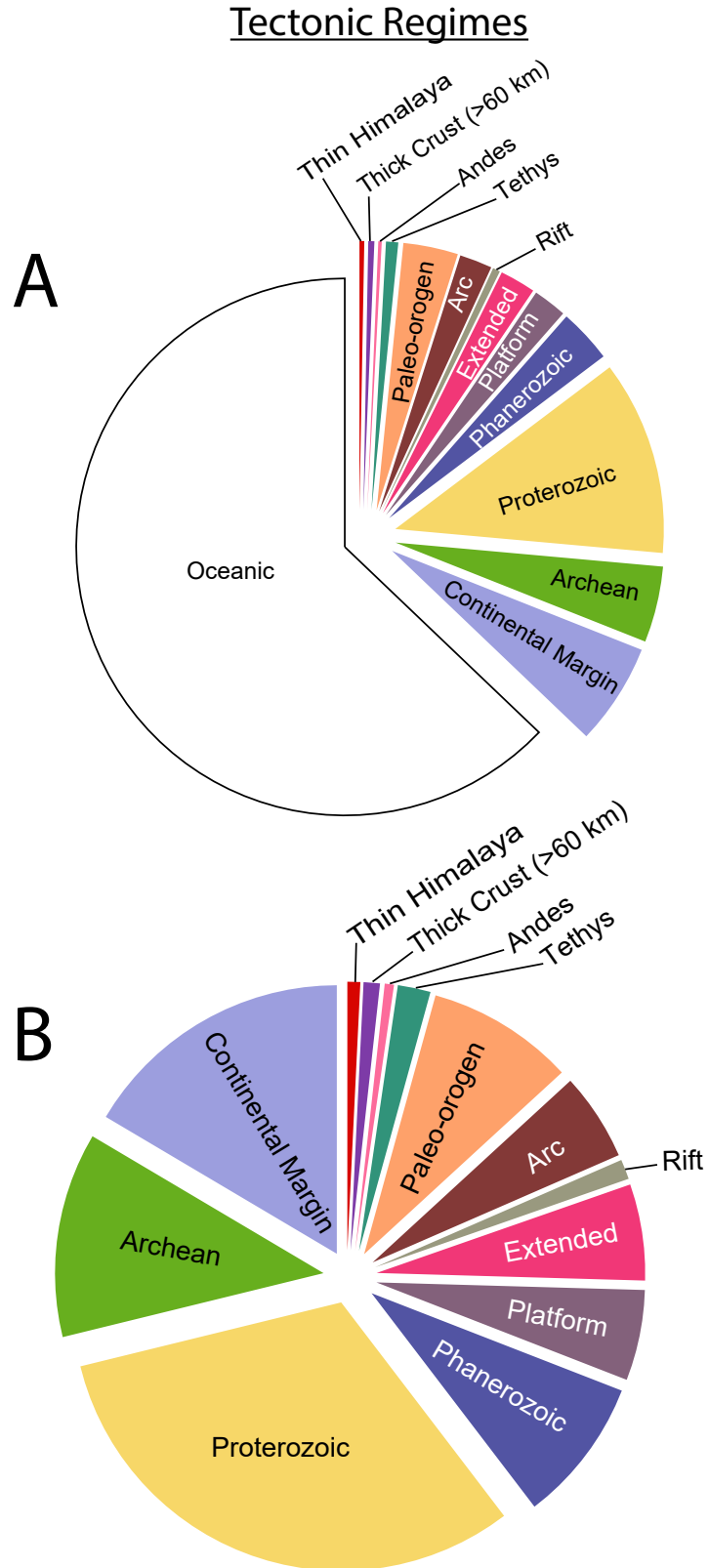


Figure 1: The weighted area proportion of crustal types, or “tectonic regimes”, used for our model as A) a fraction of total crust and B) a fraction of continental crust. Proterozoic crust is most abundant (32% of the continental crust), followed by continental margins (16%) and Archean crust (12%). Modern and paleo-orogens, including arcs, make up a combined 19% of the continental crust in our model.

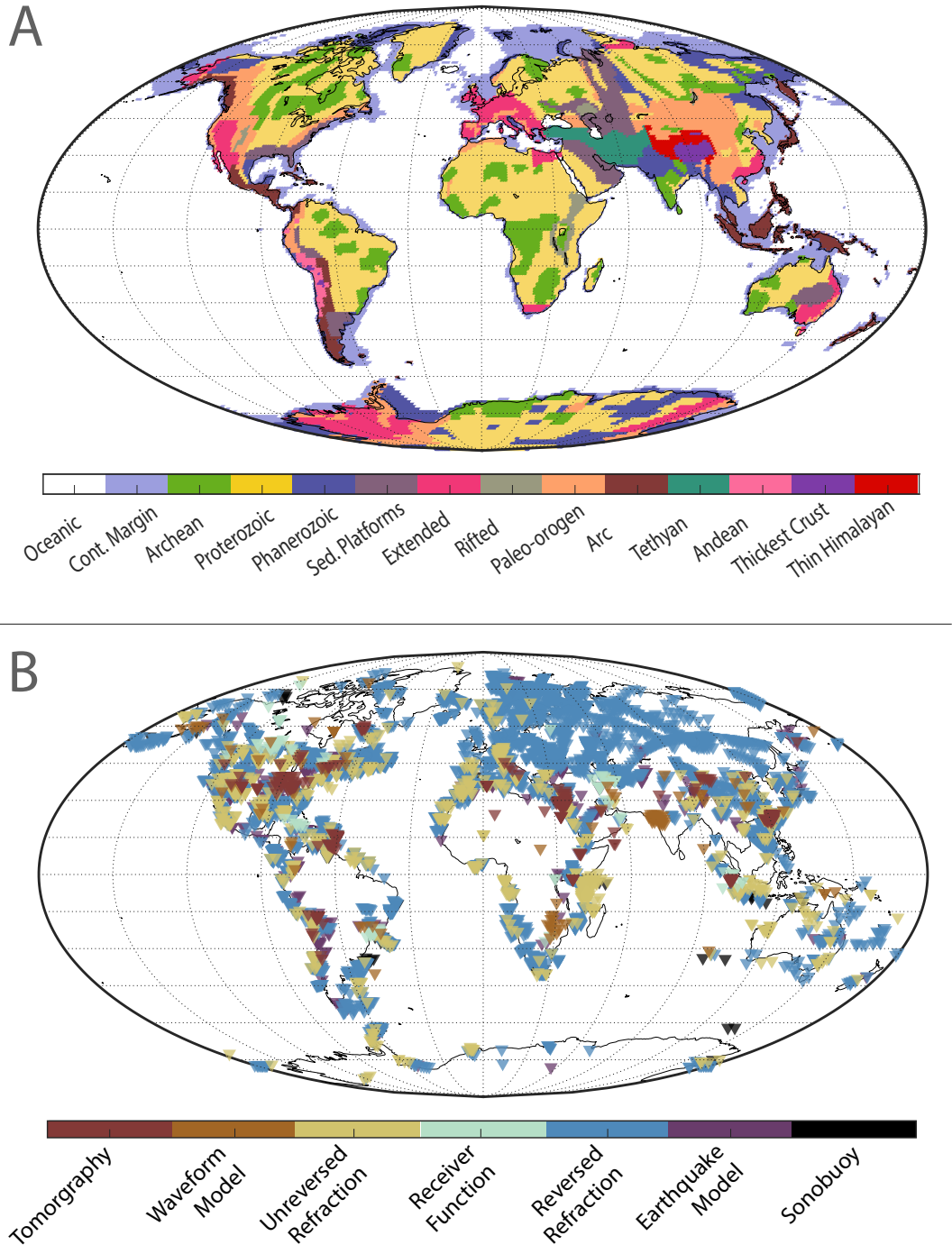


Figure 2: A) The mapped distribution of our 13 crust types and B) the seismic velocity profile data distribution from the USGS database. Data coverage is greatest in the northern hemisphere while places with less coverage, like Africa and Antarctica, rely more heavily on extrapolation of crust type.

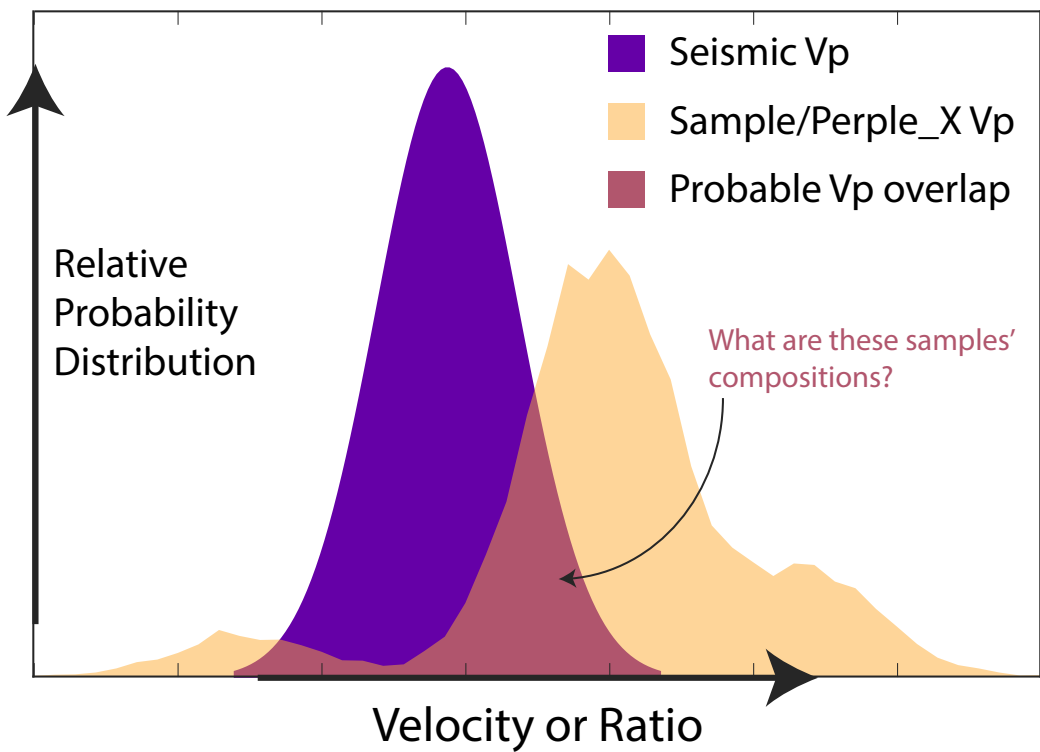


Figure 3: A conceptual illustration of overlapping velocity distributions used to identify probable crust compositions. The central pink region of the diagram, where the measured seismic velocity distribution (purple) overlaps the Perple\_X-generated velocity distribution (tan), are the velocities that are considered the best-fit by the model. The model records the compositions of the samples that can produce the best-fit velocities.

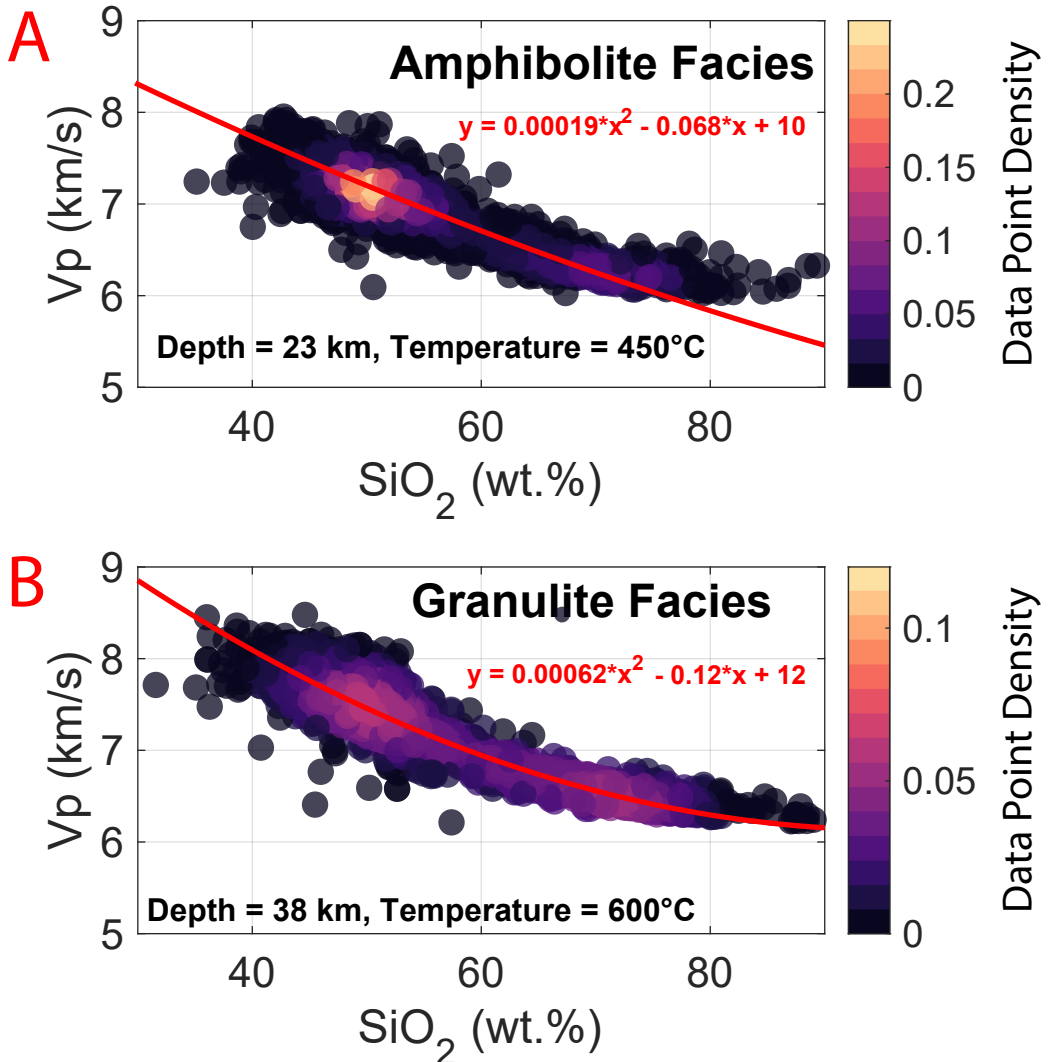


Figure 4: Vp as a function of SiO<sub>2</sub> wt.% for amphibolite (A) and granulite (B) facies lithologies at expected deep crustal pressures and temperatures. The color of the data points indicates percent data point density, with the brighter colors indicating more data points. The red line shows the best fit quadratic regression between Vp and SiO<sub>2</sub> and changes for different temperatures and pressures.

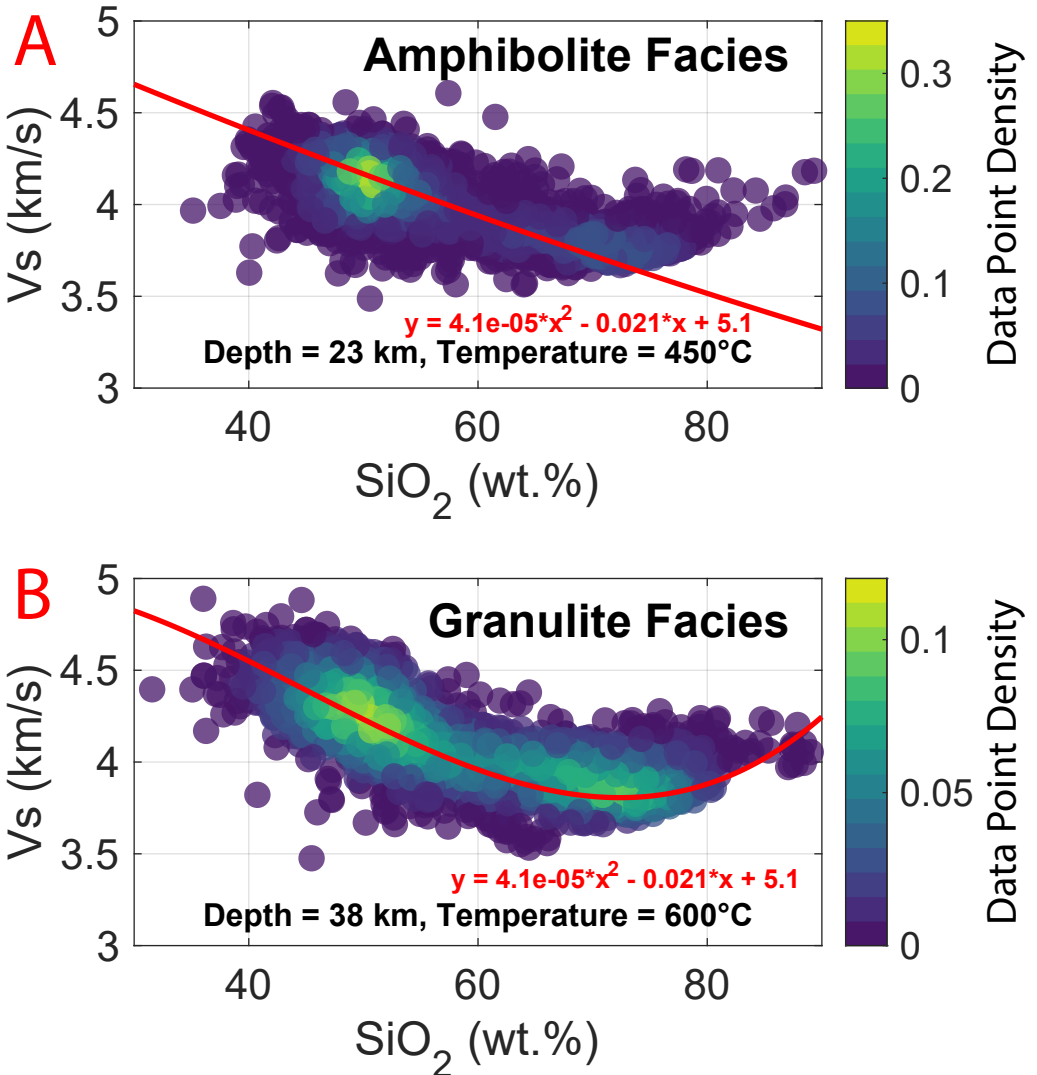


Figure 5: Vs as a function of SiO<sub>2</sub> wt.% for amphibolite (A) and granulite (B) facies lithologies at expected deep crustal pressures and temperatures, generated through Perple\_X. The color of the data points indicates percent data point density, with the brighter colors indicating more data points. The red line shows the best fit quadratic regression between Vs and SiO<sub>2</sub> and changes for different temperatures and pressures. There is more scatter between SiO<sub>2</sub> and Vs than SiO<sub>2</sub> and Vp, but can be combined for a tighter constraint on composition than either compressional or shear velocity alone.

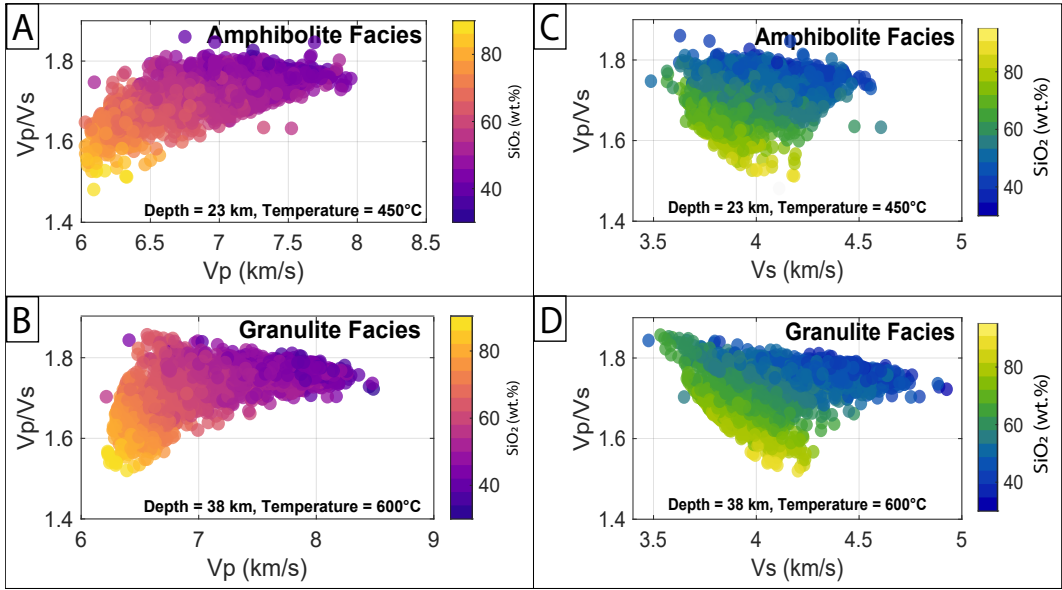


Figure 6:  $V_p/V_s$  plotted against (A)  $V_p$  and (B)  $V_s$  for amphibolite facies lithologies, and (C)  $V_p$  and (D)  $V_s$  for granulite facies lithologies at deep crustal temperatures and pressures generated through Perple\_X. Color indicates  $\text{SiO}_2$  concentration. Low  $V_p$ 's correlate to a low  $V_p/V_s$  ratio.

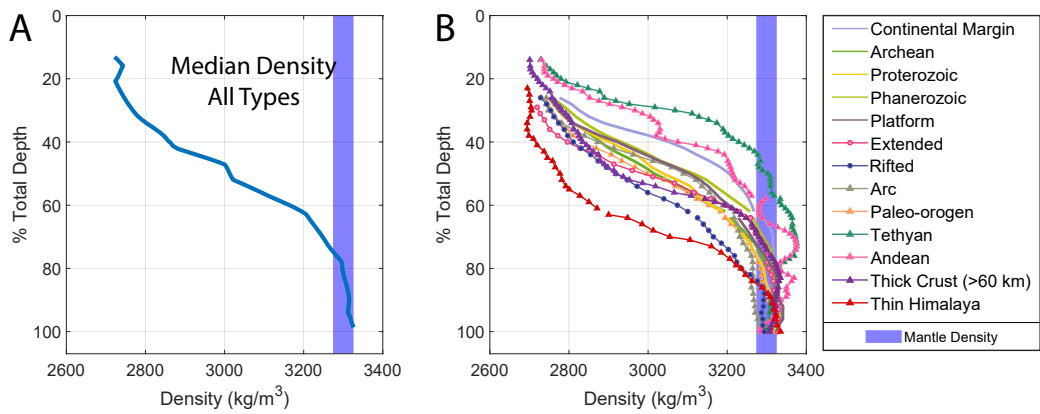


Figure 7: Calculated density normalized to depth for (A) average continental crust and (B) our different tectonic regimes with an imposed lithology transition (amphibolite to granulite facies) at 2/3 total crust depth. By this method, the bottom ~20 – 30%

of the crust approaches or exceeds mantle density.

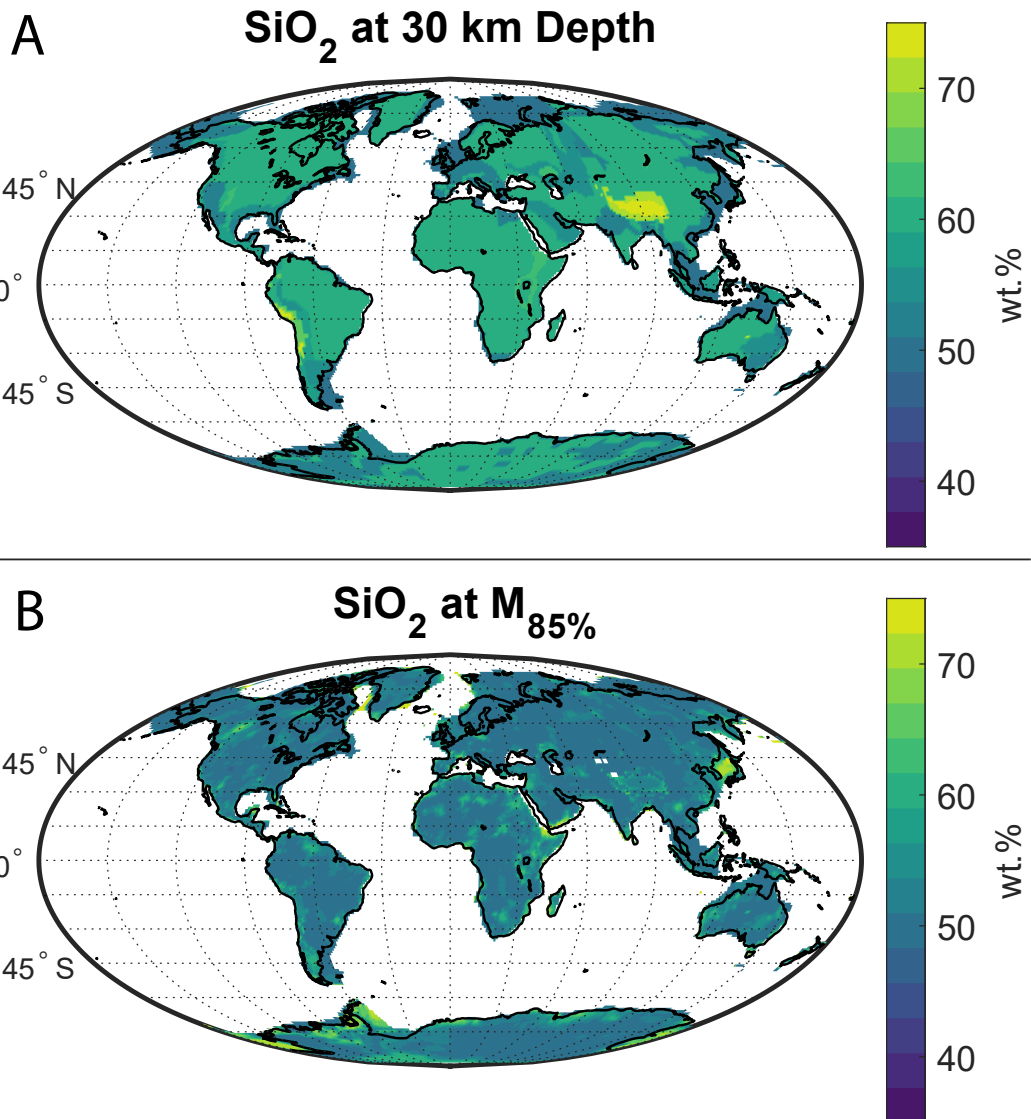


Figure 8: Global  $\text{SiO}_2$  composition at a depth of 30 km shows regional distinctions whereas measuring composition at a crustal depth relative to the Moho ( $M_{85\%}$  notation = 85% of the total crustal depth) produces a view of a deep crust that is contiguous and decreases in  $\text{SiO}_2$  gradually with depth. Areas of high projected  $\text{SiO}_2$  include the Himalayas, Andes, East African rift, and some continental margins. While the Himalayas and Andes may show compositional features, the high  $\text{SiO}_2$  in some rifts and continental margins are likely from model input inaccuracies

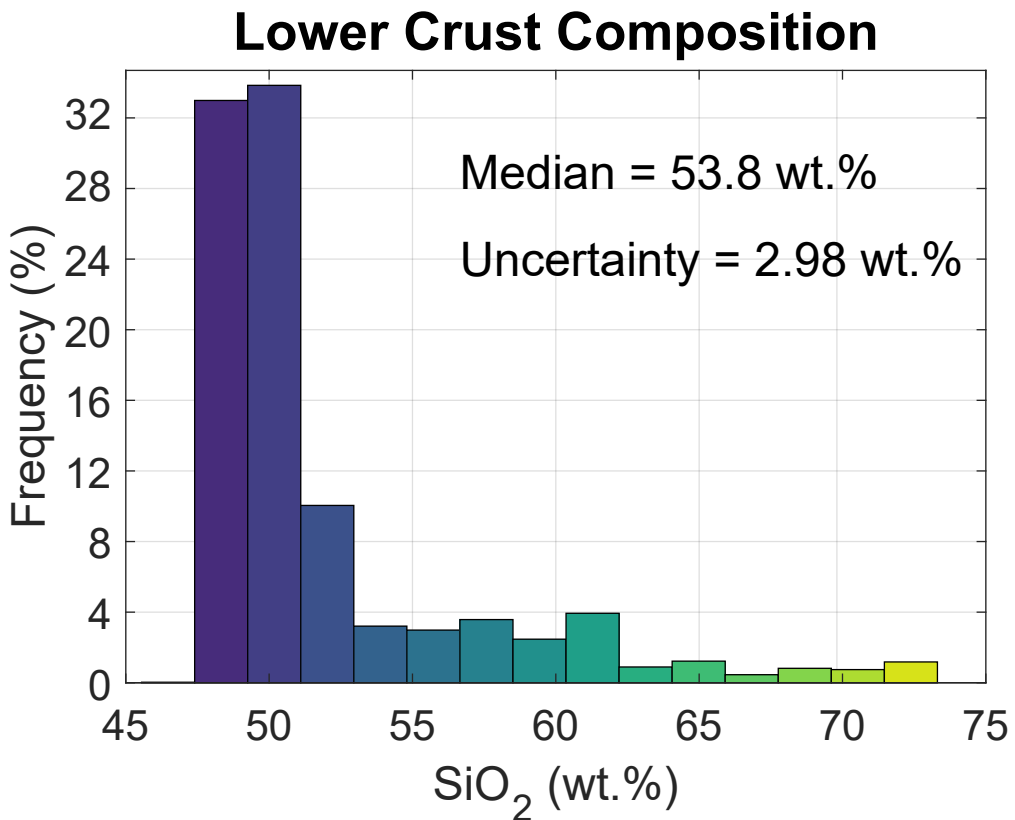


Figure 9: The area weighted distribution of  $\text{SiO}_2$  shows that global lower crust (bottom 1/3 of crust) favors values around 50 wt.% while possibly reaching as high as 70 wt.% in limited areas. The median lower crustal  $\text{SiO}_2$  is  $53.8 \pm 2.98$  wt.%, though the distribution is far from normal.

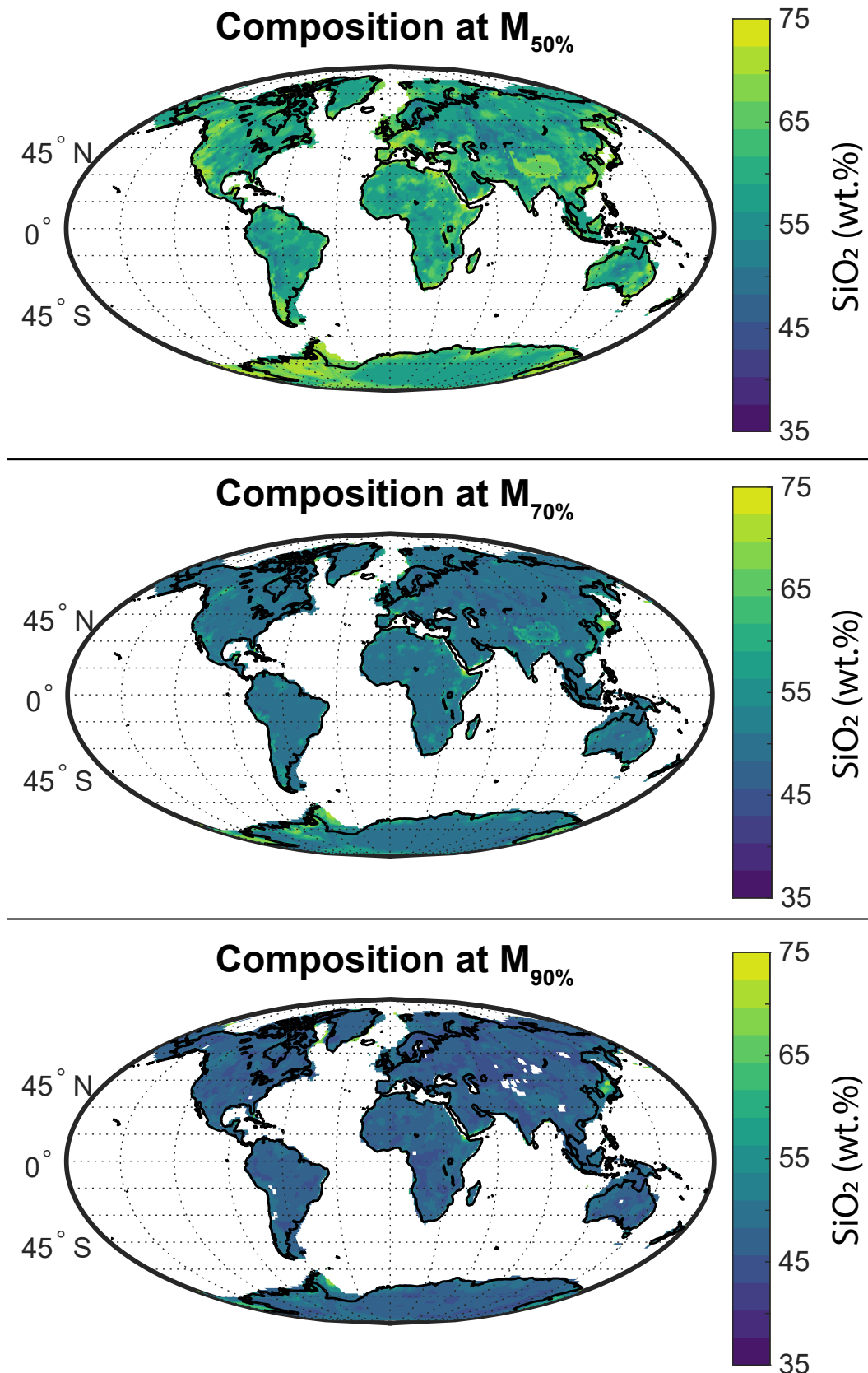


Figure 10: Global SiO<sub>2</sub> decreases with increasing depth from the middle to the bottom of the continental crust. The middle crust  $M_{50\%}$  ranges from 60 to 65 wt.% SiO<sub>2</sub> in most areas and increases at a rate of about wt.% per km until reaching the base of the crust. Uncertainties can be found in Supplemental Figure SXXX[].

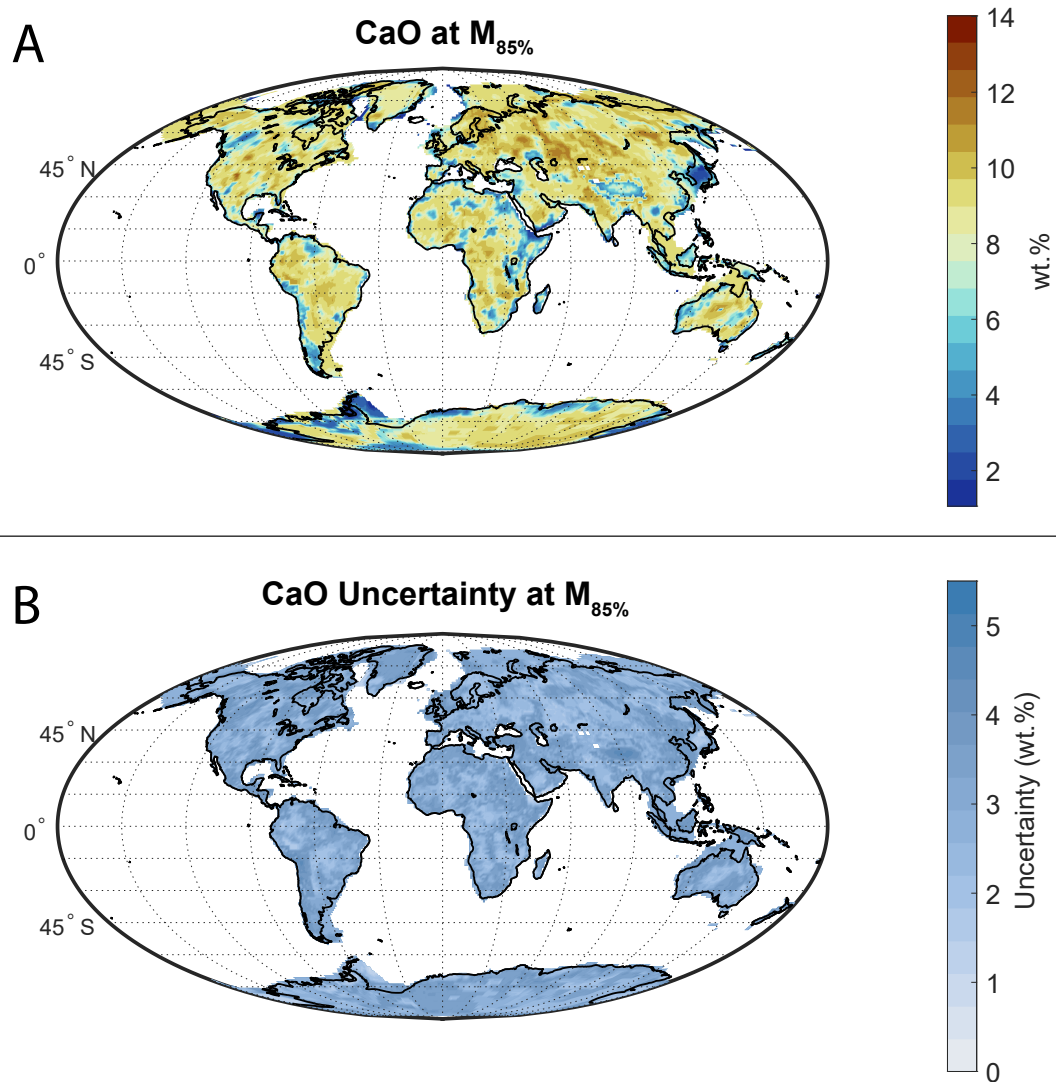


Figure 11: Global CaO abundance and uncertainty at 85% of the total crustal depth. Areas of low CaO correlate to areas of high SiO<sub>2</sub>. There does not appear to be any correlation between CaO content and uncertainty, with most regions having 3 to 4 wt.% uncertainty regardless of CaO abundance.

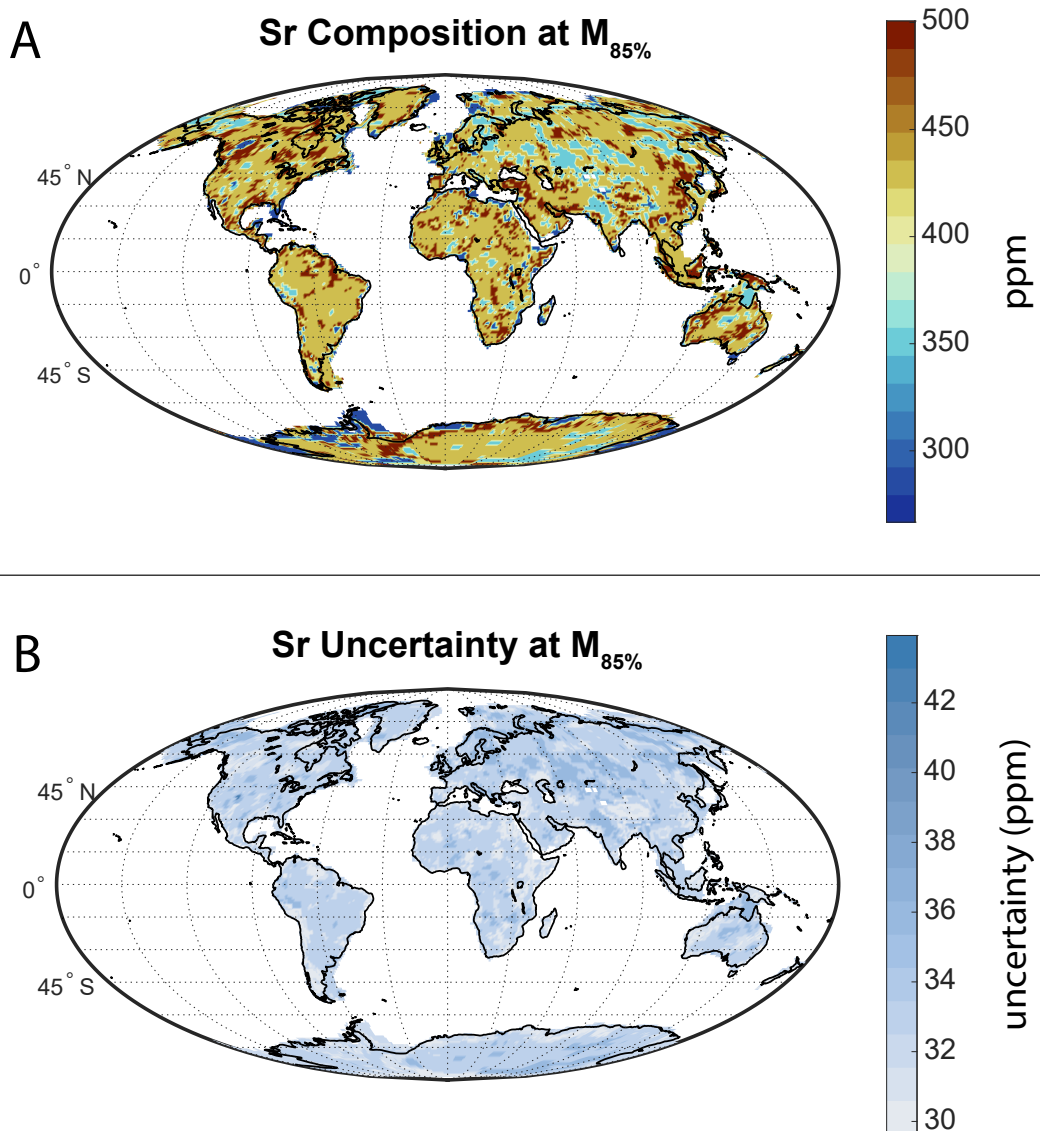


Figure 12: Global Sr abundance and uncertainty was derived from a joint probability analysis with CaO at 85% of the total crustal depth. Average global Sr abundance is  $\pm$  ppm.

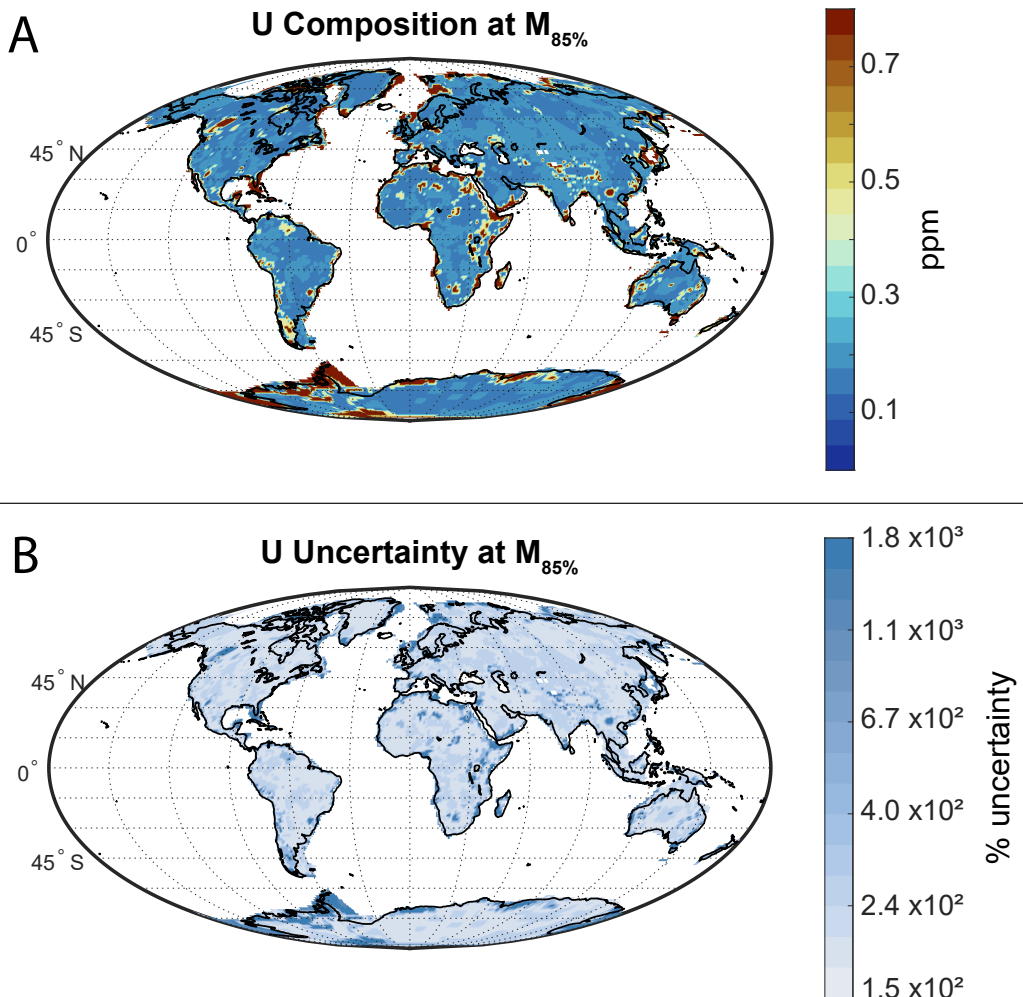


Figure 13: Global U abundance derived from a joint probability analysis with  $\text{SiO}_2$  at 85% of the total crustal depth. Uncertainties span orders of magnitude because of the range of possible U values, but the global median at this depth is  $\sim 0.2$  ppm U. Regions of high  $\text{SiO}_2$ , especially the potentially inaccurate continental margin of Antarctica correlate with high U and the highest uncertainties.

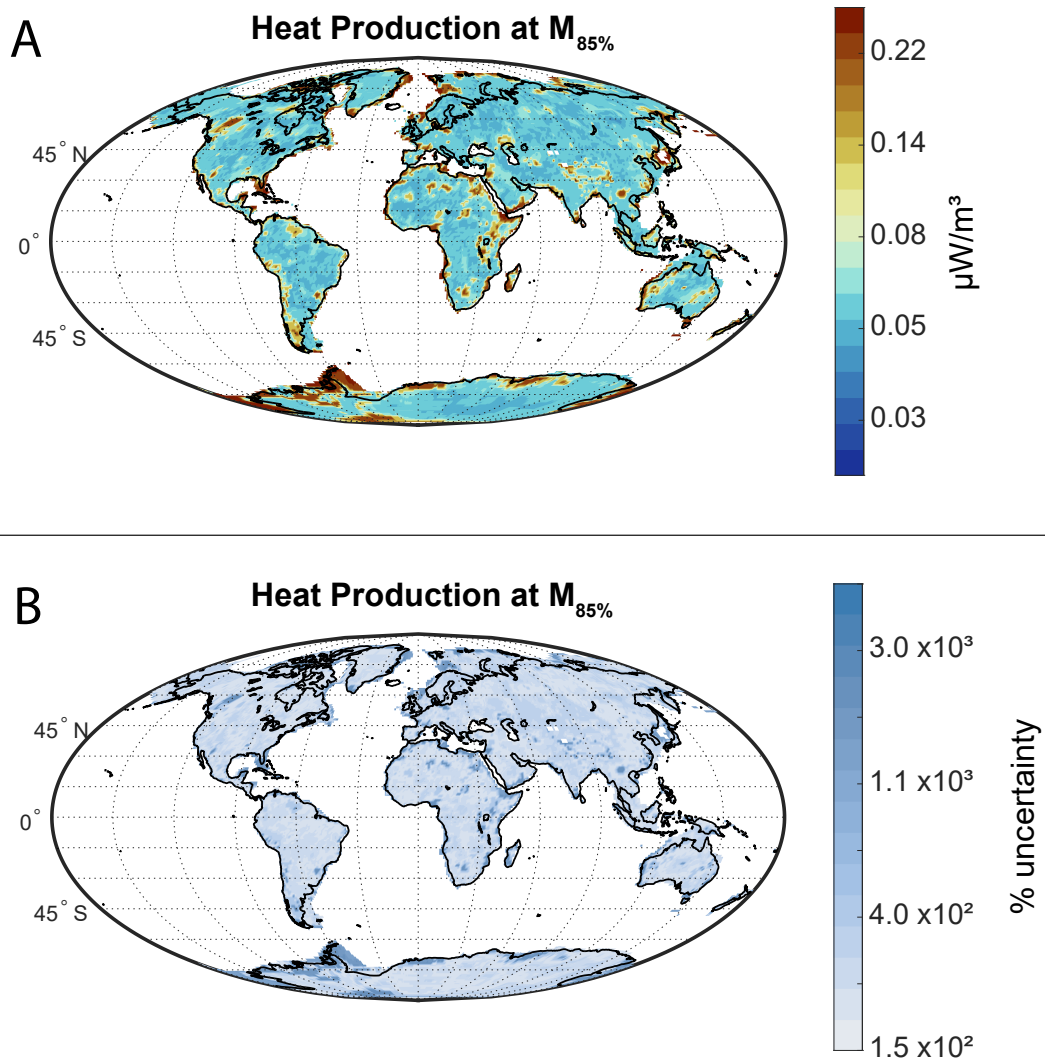


Figure 14: Global heat production at the  $M_{85\%}$  layer. The  $K_2O$  abundances were directly calculated from Perple\_X, whereas U and Th abundances were derived from relationships to  $SiO_2$  and a Th/U mass ratio of  $3.7 \pm 0.1$ . Uncertainties in U abundances dominate the overall uncertainty (see Figure 13).

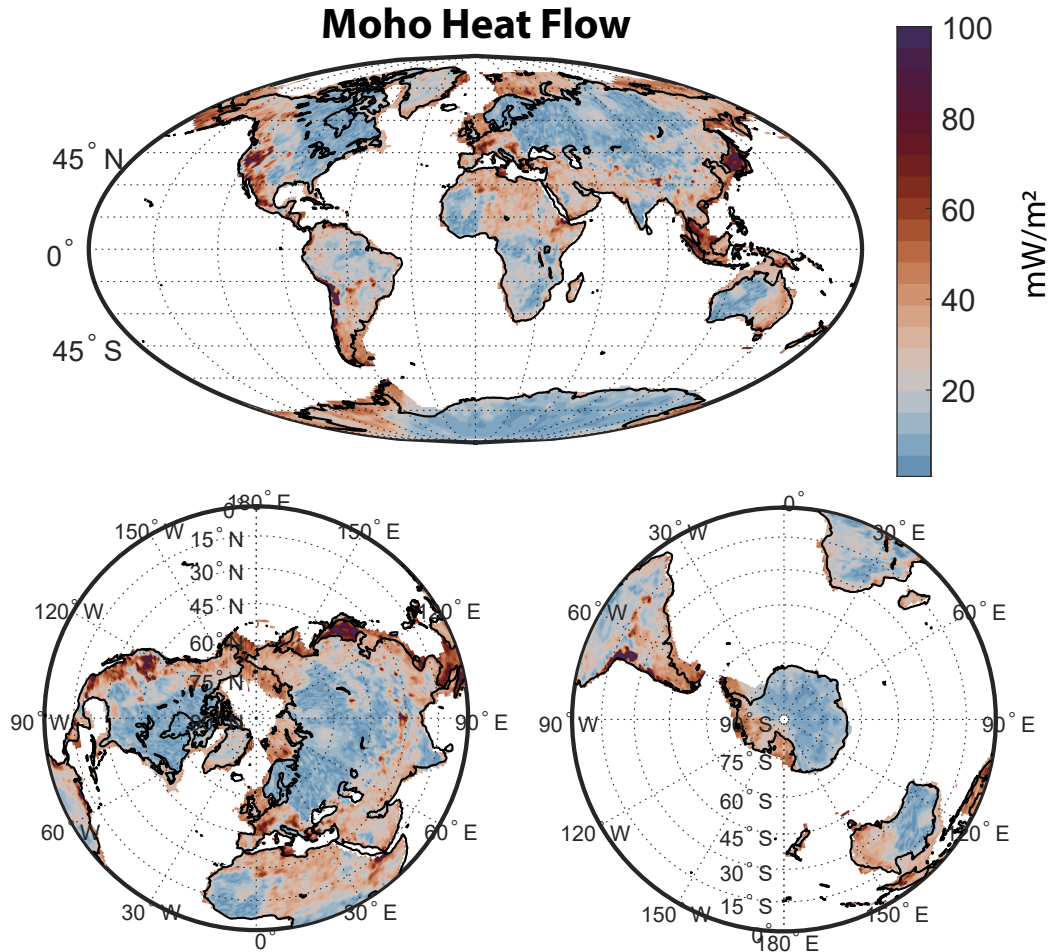


Figure 15: Global heat flux across the Moho calculated by subtracting crustal heat production from measurements of surface heat flux. The median subcontinental Moho heat flux is  $24.8 \pm 11.9$  mW/m<sup>2</sup> globally and  $18.8 \pm 8.8$  mW/m<sup>2</sup> for stable continent. This result assumes a uniform upper crustal heat production of  $0.8 \mu\text{W}/\text{m}^3$  for cratonic and  $1.65 \mu\text{W}/\text{m}^3$  for non-cratonic regions.

Table 1: Crustal Regimes by Surface Area

Crustal Regime	% All Crust	% Continental Crust	Number of Profiles
Oceanic	63	-	-
Continental Margin	6	16	1693
Archean	5	12	416
Proterozoic	12	32	919
Phanerozoic	3	9	353
Platform	2	5	318
Extended	2	6	403
Rifted	<1	1	148
Arc	2	5	262
Paleo-orogenic	3	9	565
Tethyan	<1	2	59
Andean	<1	1	31
Thick Crust	<1	1	106
Thin Himalayan	<1	1	28

Table 2: Median SiO<sub>2</sub> in wt.% for different tectonic regimes

	SiO <sub>2</sub> at $M_{50\%}$ (~middle crust)	Uncertainty ±	SiO <sub>2</sub> at $M_{85\%}$ (~lower crust)	Uncertainty ±
Continental Margin	61.1	10.2	52.8	2.7
Archean	61.0	7.8	51.9	2.9
Proterozoic	62.0	7.3	52.9	3.7
Phanerozoic	61.5	9.2	51.8	2.5
Platform	58.9	7.6	51.8	2.7
Extended	68.9	7.6	52.7	2.4
Rifted	66.8	7.3	57.8	6.5
Arc	68.7	9.8	57.6	6.9
Paleo-orogenic	63.9	9.2	52.7	3.4
Tethyan	63.9	9.4	52.3	3.1
Andean	59.9	9.1	56.0	6.9
Thick Crust	68.2	8.8	58.4	8.6
Thin Himalayan	70.7	5.9	51.3	2.2

Table 3: Middle and Lower Crust Bulk Composition in wt.%

	Composition at $M_{50\%}$ (~middle crust)	Uncertainty ±	Composition at $M_{85\%}$ (~lower crust)	Uncertainty ±
SiO <sub>2</sub>	61.2	7.31	53.8	2.98
TiO <sub>2</sub>	0.77	0.38	0.87	0.40
Al <sub>2</sub> O <sub>3</sub>	16.4	1.68	17.3	3.46
FeO	7.52	2.93	9.75	2.25
MnO	0.12	0.06	0.17	0.06
MgO	3.04	1.73	5.92	2.81
CaO	5.72	2.05	9.07	3.08
Na <sub>2</sub> O	3.77	0.81	2.28	1.02
K <sub>2</sub> O	1.46	0.97	0.81	0.96

Table 4: Continental crust composition estimates

	Christen & Mooney, 1995	Liu et al., 2001	Jagoutz & Schmidt, 2012	Rudnick & Gao, 2014	Hacker et al., 2015†	Hacker et al., 2015‡	This Study
<i>Middle Crust</i>							
SiO <sub>2</sub>	62	-	-	63.5	62.7	57.3	61.2
TiO <sub>2</sub>	-	-	-	0.69	0.8	0.99	0.77
Al <sub>2</sub> O <sub>3</sub>	-	-	-	15	15.7	16.8	16.4
FeO <sub>T</sub>	-	-	-	6.02	6.76	8.15	7.52
MnO	-	-	-	0.10	0.13	0.16	0.12
MgO	-	-	-	3.59	3.51	4.46	3.04
CaO	-	-	-	5.25	5.27	6.63	5.72
Na <sub>2</sub> O	-	-	-	3.39	3.42	3.89	3.77
K <sub>2</sub> O	-	-	-	2.3	1.6	1.42	1.46
Mg#	-	-	-	51.5	48.1	43.4	41.9
<i>Lower Crust</i>							
SiO <sub>2</sub>	47	58.3	52.16	53.4	50.7	57.3	53.8
TiO <sub>2</sub>	-	0.59	0.78	0.82	1.24	0.99	0.87
Al <sub>2</sub> O <sub>3</sub>	-	13.6	18.68	16.9	16.5	16.8	16.3
FeO <sub>T</sub>	-	5.32	8.41	8.57	10.39	8.15	9.75
MnO	-	0.08	0.17	0.10	0.19	0.16	0.17
MgO	-	9.58	5.86	7.24	7.03	4.46	5.92
CaO	-	4.54	10.79	9.59	10.1	6.63	9.07
Na <sub>2</sub> O	-	2.54	2.56	2.65	2.8	3.89	2.28
K <sub>2</sub> O	-	3.23	0.41	0.61	0.79	1.42	0.81
Mg#	-	76.2	55.4	60.1	54.7	49.4	52.0

† Hacker et al. (2015) fast Vp crustal model

‡ Hacker et al. (2015) middle crust composition = lower crust composition model

Table 5: Heat production calculation parameters

Parameter	Value
Global Surface Heat Flux	Lucazeau (2019)
Antarctica Surface Heat Flux	Shen et al. (2020)
Upper Crust Heat Production	1.65 $\mu\text{W}/\text{m}^3$ (Gaschnig et al., 2016)
Upper Crust Heat Production (cratonic)	0.8 $\mu\text{W}/\text{m}^3$ (see Discussion for source)
Average Deep Crustal Density	2900 kg/m <sup>3</sup> (Wipperfurther et al. (2020), this study)
Thermal Conductivity	2.65 W/(m*K) (Miao et al., 2014)

497      **References**

- 498      Artemieva, I. M. (2006). Global  $1 \times 1$  thermal model TC1 for the continental lithosphere:  
 499      implications for lithosphere secular evolution. *Tectonophysics*, *416*(1-4), 245–277.
- 500      Ashwal, L., Morgan, P., Kelley, S., & Percival, J. (1987). Heat production in an Archean  
 501      crustal profile and implications for heat flow and mobilization of heat-producing ele-  
 502      ments. *Earth and Planetary Science Letters*, *85*(4), 439–450.
- 503      Caldwell, W. B., Klemperer, S. L., Rai, S. S., & Lawrence, J. F. (2009). Partial melt in the  
 504      upper-middle crust of the northwest himalaya revealed by rayleigh wave dispersion.  
 505      *Tectonophysics*, *477*(1-2), 58–65.
- 506      Cammarano, F., & Guerri, M. (2017). Global thermal models of the lithosphere. *Geophysical*  
 507      *Journal International*, *210*(1), 56–72.
- 508      Cho, H.-M., Kim, H.-J., Jou, H.-T., Hong, J.-K., & Baag, C.-E. (2004). Transition from  
 509      rifted continental to oceanic crust at the southeastern korean margin in the east sea  
 510      (japan sea). *Geophysical Research Letters*, *31*(7).
- 511      Christensen, N. I., & Mooney, W. D. (1995). Seismic velocity structure and composition of  
 512      the continental crust: A global view. *Journal of Geophysical Research: Solid Earth*,  
 513      *100*(B6), 9761–9788.
- 514      Connolly, J. A. D. (2005). Computation of phase equilibria by linear programming: A tool  
 515      for geodynamic modeling and its application to subduction zone decarbonation. *Earth*  
 516      *and Planetary Science Letters*, *236*(1), 524–541. doi: 10.1016/j.epsl.2005.04.033
- 517      Ducea, M. N. (2011). Fingerprinting orogenic delamination. *Geology*, *39*(2), 191–192.
- 518      Fountain, D. M., Furlong, K. P., & Salisbury, M. H. (1987). A heat production model  
 519      of a shield area and its implications for the heat flow-heat production relationship.  
 520      *Geophysical Research Letters*, *14*(3), 283–286.
- 521      Gao, Y., Tilmann, F., van Herwaarden, D.-P., Thrastarson, S., Fichtner, A., Heit, B., ...  
 522      Schurr, B. D. (2021). Full waveform inversion beneath the central andes: Insight into  
 523      the dehydration of the nazca slab and delamination of the back-arc lithosphere. *Earth*  
 524      *and Space Science Open Archive ESSOAr*.
- 525      Gaschnig, R. M., Rudnick, R. L., McDonough, W. F., Kaufman, A. J., Valley, J. W., Hu, Z.,  
 526      ... Beck, M. L. (2016). Compositional evolution of the upper continental crust through  
 527      time, as constrained by ancient glacial diamictites. *Geochimica et Cosmochimica Acta*,  
 528      *186*, 316–343.
- 529      Gohl, K. (2008). Antarctica's continent-ocean transitions: consequences for tectonic re-  
 530      constructions. In *Antarctica: A keystone in a changing world: Proceedings of the*  
 531      *10th international symposium on antarctic earth sciences/alan k. cooper, peter barrett,*  
 532      *howard stagg, bryan storey, edmund stump, woody wise, and the 10th isaes editorial*  
 533      *team, polar research* (pp. 29–38).

- 534 Gruber, B., Chacko, T., Pearson, D. G., Currie, C., & Menzies, A. (2021). Heat production  
535 and m oho temperatures in cratonic crust: evidence from lower crustal xenoliths from  
536 the slave craton. *Lithos*, 380, 105889.
- 537 Hacker, B. R., & Abers, G. A. (2004). Subduction Factory 3: An Excel worksheet and macro  
538 for calculating the densities, seismic wave speeds, and H<sub>2</sub>O contents of minerals and  
539 rocks at pressure and temperature. *Geochemistry, Geophysics, Geosystems*, 5(1). doi:  
540 10.1029/2003GC000614
- 541 Hacker, B. R., Kelemen, P. B., & Behn, M. D. (2015). Continental lower crust. *Annual  
542 Review of Earth and Planetary Sciences*, 43, 167–205.
- 543 Hartmann, J., Dürr, H. H., Moosdorf, N., Meybeck, M., & Kempe, S. (2012). The geo-  
544 chemical composition of the terrestrial surface (without soils) and comparison with the  
545 upper continental crust. *International Journal of Earth Sciences*, 101(1), 365–376.
- 546 Hirata, N., Karp, B. Y., Yamaguchi, T., Kanazawa, T., Suyehiro, K., Kasahara, J., ...  
547 Kinoshita, H. (1992). Oceanic crust in the japan basin of the japan sea by the 1990  
548 japan-ussr expedition. *Geophysical Research Letters*, 19(20), 2027–2030.
- 549 Holland, T. J. B., & Powell, R. (2004). An internally consistent thermodynamic data set  
550 for phases of petrological interest: An Internally Consistent Thermodynamic Dataset.  
551 *Journal of Metamorphic Geology*, 16(3), 309–343. doi: 10.1111/j.1525-1314.1998.00140  
552 .x
- 553 Huang, Y., Chubakov, V., Mantovani, F., Rudnick, R. L., & McDonough, W. F. (2013). A  
554 reference Earth model for the heat-producing elements and associated geoneutrino flux.  
555 *Geochemistry, Geophysics, Geosystems*, 14(6), 2003–2029. doi: 10.1002/ggge.20129
- 556 Jagoutz, O., Müntener, O., Schmidt, M. W., & Burg, J.-P. (2011). The roles of flux-and  
557 decompression melting and their respective fractionation lines for continental crust  
558 formation: Evidence from the kohistan arc. *Earth and Planetary Science Letters*,  
559 303(1-2), 25–36.
- 560 Jagoutz, O., & Schmidt, M. W. (2012). The formation and bulk composition of modern  
561 juvenile continental crust: The kohistan arc. *Chemical Geology*, 298, 79–96.
- 562 Jaupart, C., Mareschal, J., & Watts, A. (2007). Heat flow and thermal structure of the  
563 lithosphere. *Treatise on geophysics*, 6, 217–252.
- 564 Jaupart, C., Mareschal, J.-C., Bouquerel, H., & Phaneuf, C. (2014). The building and  
565 stabilization of an archean craton in the superior province, canada, from a heat flow  
566 perspective. *Journal of Geophysical Research: Solid Earth*, 119(12), 9130–9155.
- 567 Jaupart, C., Mareschal, J.-C., & Iarotsky, L. (2016). Radiogenic heat production in the  
568 continental crust. *Lithos*, 262, 398–427.
- 569 Kay, R. W., & Kay, S. M. (1993). Delamination and delamination magmatism. *Tectono-  
570 physics*, 219(1-3), 177–189.

- 571 Kukkonen, I., Golovanova, I., Khachay, Y. V., Druzhinin, V., Kosarev, A., & Schapov,  
572 V. (1997). Low geothermal heat flow of the urals fold belt—implication of low heat  
573 production, fluid circulation or palaeoclimate? *Tectonophysics*, 276(1-4), 63–85.
- 574 Liu, Y.-S., Gao, S., Jin, S.-Y., Hu, S.-H., Sun, M., Zhao, Z.-B., & Feng, J.-L. (2001).  
575 Geochemistry of lower crustal xenoliths from neogene hannuoba basalt, north china  
576 craton: Implications for petrogenesis and lower crustal composition. *Geochimica et  
577 Cosmochimica Acta*, 65(15), 2589–2604.
- 578 Lucazeau, F. (2019). Analysis and mapping of an updated terrestrial heat flow data set.  
579 *Geochemistry, Geophysics, Geosystems*, 20(8), 4001–4024.
- 580 Mareschal, J.-C., & Jaupart, C. (2013). Radiogenic heat production, thermal regime and  
581 evolution of continental crust. *Tectonophysics*, 609, 524–534.
- 582 McCarthy, A., Falloon, T., Sauermilch, I., Whittaker, J., Niida, K., & Green, D. (2020).  
583 Revisiting the australian-antarctic ocean-continent transition zone using petrological  
584 and geophysical characterization of exhumed subcontinental mantle. *Geochemistry,  
585 Geophysics, Geosystems*, 21(7), e2020GC009040.
- 586 Miao, S. Q., Li, H. P., & Chen, G. (2014). Temperature dependence of thermal diffusivity,  
587 specific heat capacity, and thermal conductivity for several types of rocks. *Journal of  
588 Thermal Analysis and Calorimetry*, 115(2), 1057–1063.
- 589 Mooney, W. D. (2015). *Crust and lithospheric structure—global crustal structure* (Vol. 1;  
590 G. Schubert, Ed.). Oxford: Elsevier.
- 591 Mooney, W. D., Laske, G., & Masters, T. G. (1998). Crust 5.1: A global crustal model at  
592 5 × 5. *Journal of Geophysical Research: Solid Earth*, 103(B1), 727–747.
- 593 Nelson, K. D., Zhao, W., Brown, L., Kuo, J., Che, J., Liu, X., ... others (1996). Partially  
594 molten middle crust beneath southern tibet: synthesis of project indepth results.  
595 *Science*, 274(5293), 1684–1688.
- 596 Nyblade, A. A., & Pollack, H. N. (1993). A global analysis of heat flow from precambrian  
597 terrains: implications for the thermal structure of archean and proterozoic lithosphere.  
598 *Journal of Geophysical Research: Solid Earth*, 98(B7), 12207–12218.
- 599 Pasyanos, M. E., Masters, T. G., Laske, G., & Ma, Z. (2014). LITHO1.0: An updated crust  
600 and lithospheric model of the Earth. *Journal of Geophysical Research: Solid Earth*,  
601 119(3), 2153–2173. doi: 10.1002/2013JB010626
- 602 Phaneuf, C., & Mareschal, J.-C. (2014). Estimating concentrations of heat producing ele-  
603 ments in the crust near the sudbury neutrino observatory, ontario, canada. *Tectono-  
604 physics*, 622, 135–144.
- 605 Pinet, C., & Jaupart, C. (1987). The vertical distribution of radiogenic heat production in  
606 the precambrian crust of norway and sweden: geothermal implications. *Geophysical  
607 Research Letters*, 14(3), 260–263.

- 608 Regis, D., Warren, C., Mottram, C. M., & Roberts, N. M. (2016). Using monazite and  
 609 zircon petrochronology to constrain the P–T–t evolution of the middle crust in the  
 610 bhutan himalaya. *Journal of Metamorphic Geology*, 34(6), 617–639.
- 611 Ries, J., Bettadpur, S., Eanes, R., Kang, Z., Ko, U.-d., McCullough, C., ... others (2016).  
 612 *The development and evaluation of the global gravity model ggm05* (Tech. Rep.). Center  
 613 for Space Research, Report number: CSR-16-02 NASA.
- 614 Rudnick, R. L., & Gao, S. (2014). Composition of the Continental Crust. In *Treatise on*  
 615 *Geochemistry* (p. 1-51). Elsevier. doi: 10.1016/B978-0-08-095975-7.00301-6
- 616 Rudnick, R. L., & Nyblade, A. A. (1999). The thickness and heat production of archean  
 617 lithosphere: constraints from xenolith thermobarometry and surface heat flow. *Mantle*  
 618 *petrology: field observations and high pressure experimentation: a tribute to Francis*  
 619 *R.(Joe) Boyd*, 6, 3–12.
- 620 Sammon, L. G., Gao, C., & McDonough, W. F. (2020). Lower crustal composition in the  
 621 southwestern united states. *Journal of Geophysical Research: Solid Earth*, 125(3),  
 622 e2019JB019011.
- 623 Sammon, L. G., & McDonough, W. F. (2021). A geochemical review of amphibolite,  
 624 granulite, and eclogite facies lithologies: Perspectives on the deep continental crust.
- 625 Schilling, F., & Partzsch, G. (2001). Quantifying partial melt fraction in the crust beneath  
 626 the central andes and the tibetan plateau. *Physics and Chemistry of the Earth, Part*  
 627 *A: Solid Earth and Geodesy*, 26(4-5), 239–246.
- 628 Schmitz, M., Heinsohn, W.-D., & Schilling, F. (1997). Seismic, gravity and petrological  
 629 evidence for partial melt beneath the thickened central andean crust (21–23 s).  
 630 *Tectonophysics*, 270(3-4), 313–326.
- 631 Searle, M., Cottle, J., Streule, M., & Waters, D. (2009). Crustal melt granites and  
 632 migmatites along the himalaya: melt source, segregation, transport and granite em-  
 633 placement mechanisms. *Earth and Environmental Science Transactions of the Royal*  
 634 *Society of Edinburgh*, 100(1-2), 219–233.
- 635 Semprich, J., & Simon, N. S. C. (2014). Inhibited eclogitization and consequences for  
 636 geophysical rock properties and delamination models: Constraints from cratonic lower  
 637 crustal xenoliths. *Gondwana Research*, 25(2), 668–684. doi: 10.1016/j.gr.2012.08.018
- 638 Shen, W., Wiens, D. A., Lloyd, A. J., & Nyblade, A. A. (2020). A geothermal heat flux  
 639 map of antarctica empirically constrained by seismic structure. *Geophysical Research*  
 640 *Letters*, 47(14), e2020GL086955.
- 641 Stixrude, L., & Lithgow-Bertelloni, C. (2011). Thermodynamics of mantle minerals-ii. phase  
 642 equilibria. *Geophysical Journal International*, 184(3), 1180–1213.
- 643 Szwilus, W., Afonso, J. C., Ebbing, J., & Mooney, W. D. (2019). Global crustal thick-  
 644 ness and velocity structure from geostatistical analysis of seismic data. *Journal of*

- 645           *Geophysical Research: Solid Earth*, 124(2), 1626-1652.
- 646   Wilkinson, B. H., McElroy, B. J., Kesler, S. E., Peters, S. E., & Rothman, E. D. (2009).
- 647           Global geologic maps are tectonic speedometers—rates of rock cycling from area-age
- 648           frequencies. *Geological Society of America Bulletin*, 121(5-6), 760–779.
- 649   Wipperfurth, S. A., Guo, M., Šrámek, O., & McDonough, W. F. (2018). Earth's chondritic
- 650           Th/U: Negligible fractionation during accretion, core formation, and crust–mantle
- 651           differentiation. *Earth and Planetary Science Letters*, 498, 196-202. doi: 10.1016/j.epsl.2018.06.029
- 653   Wipperfurth, S. A., Šrámek, O., & McDonough, W. F. (2020). Reference models for
- 654           lithospheric geoneutrino signal. *Journal of Geophysical Research: Solid Earth*, 125(2),
- 655           e2019JB018433.